Journal of High Energy Astrophysics 44 (2024) 323–339

Contents lists available at ScienceDirect

Journal of High Energy Astrophysics

journal homepage: www.elsevier.com/locate/jheap

Towards a new model-independent calibration of Gamma-Ray Bursts

Arianna Favale [a,b,*], Maria Giovanna Dainotti [c,d,e,f], Adrià Gómez-Valent [b], Marina Migliaccio [a]

[a] Dipartimento di Fisica and INFN Sezione di Roma 2, Università di Roma Tor Vergata, via della Ricerca Scientifica 1, Roma, 00133, Italy
[b] Departament de Física Quàntica i Astrofísica and Institut de Ciències del Cosmos, Universitat de Barcelona, Av. Diagonal 647, Barcelona, 08028, Spain
[c] Division of Science, National Astronomical Observatory of Japan, 2-21-1 Osawa, Mitaka, Tokyo, 181-8588, Japan
[d] The Graduate University for Advanced Studies (SOKENDAI), Shonankokusaimura, Hayama, Miura District, Kanagawa, 240-0115, Japan
[e] Space Science Institute, 4765 Walnut St Ste B, Boulder, CO 80301, USA
[f] Nevada Center for Astrophysics, University of Nevada, 4505 Maryland Parkway, Las Vegas, NV 89154, USA

ARTICLE INFO

Keywords:
Gamma-ray burst
Distance scale
Cosmological parameters

ABSTRACT

Current data on baryon acoustic oscillations and Supernovae of Type Ia (SNIa) cover up to $z \sim 2.5$. These low-redshift observations play a very important role in the determination of cosmological parameters and have been widely used to constrain the ΛCDM and models beyond the standard, such as the ones with open curvature. To extend this investigation to higher redshifts, Gamma-Ray Bursts (GRBs) stand out as one of the most promising observables. In spite of being transient, they are extremely energetic and can be used to probe the universe up to $z \sim 9.4$. They exhibit characteristics that suggest they are potentially standardizable candles and this allows their use to extend the distance ladder beyond SNIa. The use of GRB correlations is still a challenge due to the spread in their intrinsic properties. One of the correlations that can be employed for the standardization is the fundamental plane relation between the peak prompt luminosity, the rest-frame end time of the plateau phase, and its corresponding luminosity, also known as the *three-dimensional Dainotti correlation*. In this work, we propose an innovative method of calibration of the Dainotti relation which is independent of cosmology. We employ state-of-the-art data on Cosmic Chronometers (CCH) at $z \lesssim 2$ and use the Gaussian Processes Bayesian reconstruction tool. To match the CCH redshift range, we select 20 long GRBs in the range $0.553 \leq z \leq 1.96$ from the *Platinum sample*, which consists of well-defined GRB plateau properties that obey the fundamental plane relation. To ensure the generality of our method, we verify that the choice of priors on the parameters of the Dainotti relation and the modeling of CCH uncertainties and covariance have negligible impact on our results. Moreover, we consider the case in which the redshift evolution of the physical features of the plane is accounted for. We find that the use of CCH allows us to identify a sub-sample of GRBs that adhere even more closely to the fundamental plane relation, with an intrinsic scatter of $\sigma_{int} = 0.20^{+0.03}_{-0.05}$ obtained in this analysis when evolutionary effects are considered. In an epoch in which we strive to reduce uncertainties on the variables of the GRB correlations in order to tighten constraints on cosmological parameters, we have found a novel model-independent approach to pinpoint a sub-sample that can thus represent a valuable set of standardizable candles. This allows us to extend the cosmic distance ladder presenting a new catalog of calibrated luminosity distances up to $z = 5$.

1. Introduction

Standard candles constitute a well-established tool to measure cosmic distances in our universe, which in turn are used to constrain cosmological parameters of fundamental importance. They played a pivotal role in the discovery of the late-time cosmic acceleration (Riess et al., 1998; Perlmutter et al., 1999) and in the last years have proved also relevant in the discussion of the Hubble tension (Riess et al., 2022). Nowadays, the mismatch between Hubble parameter values estimated independently by late- and early-time probes through the direct and inverse distance ladders has reached the $\approx 4\sigma - 6\sigma$ level depending on the particular data set used (see Verde et al., 2019; Di Valentino et al., 2021a; Dainotti et al., 2021; Perivolaropoulos and Skara, 2022; Abdalla et al., 2022; Dainotti et al., 2022e; Riess and Breuval, 2022; Verde et al., 2023 for dedicated reviews). There exists a large redshift gap between measurements of Baryon Acoustic Oscillations (BAO) and Supernovae of Type Ia (SNIa), which cover up to $z \sim 2.5$, and CMB observations, which also encode information from the last-scattering surface

* Corresponding author.
E-mail addresses: afavale@roma2.infn.it (A. Favale), maria.dainotti@nao.ac.jp (M.G. Dainotti), agomezvalent@icc.ub.edu (A. Gómez-Valent), migliaccio@roma2.infn.it (M. Migliaccio).

https://doi.org/10.1016/j.jheap.2024.10.010
Received 18 August 2024; Received in revised form 12 October 2024; Accepted 13 October 2024
Available online 17 October 2024
2214-4048/© 2024 The Author(s). Published by Elsevier B.V. This is an open access article under the CC BY license (http://creativecommons.org/licenses/by/4.0/).

($z \sim 1100$) and beyond. Data in that gap could enhance our understanding about the underlying physical mechanism responsible for the expansion of the universe. They might be crucial to understand the origin of the cosmological tensions (see e.g. Gómez-Valent et al., 2024), including the anomalous existence of very massive galaxies in the early universe (Labbe et al., 2023). Moreover, recently a mismatch has been found between ΛCDM predictions and the Hubble diagram built out from high-z quasars (QSOs) (Risaliti and Lusso, 2019; Lusso et al., 2019; Bargiacchi et al., 2021; Signorini et al., 2023), which have been employed as standardizable candles (Risaliti and Lusso, 2015, 2017; Lusso et al., 2020; Dainotti et al., 2022f; Colgáin et al., 2022; Lenart et al., 2023; Dainotti et al., 2023; Bargiacchi et al., 2023). Therefore, it has now become necessary to extend the research to new cosmological probes at intermediate redshifts, which can come to our aid, widening the unexplored range of redshifts and serving as distance indicators. Exploring higher z requires observing more luminous objects than SNIa. This can be the case not only of QSOs, which reach up to $z \sim 7.5$ (Banados et al., 2018), but also of Gamma-Ray Bursts (GRBs), the most intense explosions in the universe after the Big Bang. These objects have been detected up to $z \sim 9.4$ so far (Cucchiara et al., 2011), but their observation might reach $z \sim 20$ (Lamb, 2003). The great advantage of the use of GRBs is their coverage at much higher redshifts than SNIa and BAO. Hence, it is important to improve their calibration in the range where other sources are present.

To standardize GRBs and use them as cosmological tools, it is necessary to find tight and intrinsic relationships, not induced by selection biases, between parameters of their light curves (or spectra) and their luminosity (or energy). In particular, in this work, we will focus on the relation involving the features of the plateau emission phase, that is, the luminosity at the end of the plateau emission and its rest frame duration (Dainotti et al., 2008, 2010, 2011a, 2013a, 2017b, 2020b, 2022d). This two-dimensional (2D) relation has been used as a cosmological tool for 15 years (Cardone et al., 2009, 2010; Dainotti et al., 2013b). However, considering three or more parameters could lead to tighter correlations. One of these correlations is the so-called *three-dimensional (3D) Dainotti relation*. It relates the peak prompt luminosity, the rest-frame end time of the plateau, and its corresponding luminosity (Dainotti et al., 2008, 2016, 2017a). The main advantages of using the Dainotti relation are that it is supported by a fundamental physical process, the magnetar emission (Rowlinson et al., 2014; Bernardini, 2015; Rea et al., 2015; Stratta et al., 2018; Dall'Osso et al., 2023), and it overcomes selection biases that could invalidate the reliability of the relations themselves (Dainotti et al., 2013a, 2017b). Moreover, prompt-afterglow relations present a reduced scatter in the afterglow features compared to more varied prompt emission properties (Dainotti et al., 2022b). This is yet another reason why using the plateau emission for standardizing GRBs might be more recommended. There are many correlations that help broaden our understanding of GRBs and their possible application as a cosmological tool. For instance, the $E_p - E_{iso}$ Amati correlation connects the spectral peak energy in the GRB cosmological rest frame and the isotropic equivalent radiated energy (Amati et al., 2002, 2008). Yonetoku et al. (2004) correlated E_p instead with the peak luminosity, L_p; this is called in the literature the Yonetoku relation. Norris et al. (2000) has also established a relation between L_p and the spectrum lag, the so-called $L_p - \tau_{lag}$ relation, and the bulk Lorentz factor in the context of the GRB fireball scenario is also found to correlate with E_{iso} (Liang et al., 2010) or with L_{iso} (Ghirlanda et al., 2012). However, the issue with many of these correlations is that they have not been demonstrated to be reliable after the truncation and selection effect tests, and when these corrections are applied, the dispersion of the relation itself increases (Collazzi et al., 2012; Heussaff et al., 2013; Petrosian et al., 2015). The source of this scatter is due to both instrumental biases and the underlying mechanism that governs the GRB emission, such as the energy and frequency at which it occurs. Indeed, the physical meaning of many of these relations is still under debate after many years since more than one interpretation is often viable, showing that the emission processes that rule GRBs still need further investigations. All these aspects might significantly limit the applicability of such relations for cosmological purposes. We refer the reader to Dainotti and Amati (2018) for a discussion on selection and instrumental biases and to Dainotti et al. (2018) or Parsotan and Ito (2022) for a comprehensive review of the several correlations existing in the literature and their possible physical explanation.

So far, GRBs data and their correlations have been used for many applications in cosmology, such as the investigation of the components of our universe, the nature of dark energy, and the Hubble constant tension (see, e.g., Amati et al., 2019; Khadka and Ratra, 2020; Khadka et al., 2021; Cao et al., 2022a). However, if a cosmological model is assumed when calibrating GRBs (or other standardizable objects, like SNIa), the so-called *circularity problem* (Ghisellini et al., 2005; Ghirlanda et al., 2006; Wang et al., 2015) can be encountered if the resulting correlations are then used to constrain parameters of models different from the one employed in the calibration. Up to now, two solutions have been proposed to overcome this problem. One is to fit simultaneously the correlation parameters and the parameters of a cosmological model of interest using GRB data (Ghirlanda et al., 2004; Li et al., 2008; Amati et al., 2008; Postnikov et al., 2014; Cao et al., 2022a,b; Dainotti et al., 2022a). In this way, cosmological constraints are uniquely determined by GRBs.

On the other hand, based on the idea of the distance ladder, one can calibrate GRBs with low-redshift probes, such as calibrated SNIa (Liang et al., 2008; Postnikov et al., 2014), given that objects at the same redshift should have the same luminosity distance regardless of the underlying cosmology if the latter respects the cosmological principle (CP). The distance ladder measurement is basically model-independent since it only relies on the CP and the assumption that SNIa are good standardizable objects, i.e., with a standardized absolute magnitude that remains constant from our vicinity to the far end of the cosmic ladder. One uses other standard candles, such as Cepheids (Riess et al., 2021) or the Tip of the Red Giant Branch (Freedman et al., 2020; Freedman, 2021; Freedman and Madore, 2023) in the lower rungs of the ladder to calibrate the SNIa, and then uses SNIa to calibrate GRBs in a model-independent way. Most of the calibrated-GRB cosmological analyses are based on this idea. They make use of cosmographical methods (Luongo and Muccino, 2020; Mu et al., 2023) or Gaussian Processes (GP) as in Liang et al. (2022). The calibration occurs at $z \lesssim 2.5$ (i.e. below the maximum redshift in the SNIa samples) and then the calibrated GRB relations can be employed to build an extended Hubble diagram up to the high-z region covered by the GRBs. In doing so, analogously to the calibration of SNIa, it is usually assumed that the GRB correlation does not evolve with redshift, although this evolution could actually have a non-negligible impact (Kumar et al., 2023). For a discussion on how different is the calibration of GRBs on SNIa or independent from SNIa and how the evolution impacts the outcome see Dainotti et al. (2013a); Dainotti and Del Vecchio (2017); Dainotti et al. (2022a). Another possible caveat of this method is that some unaccounted-for systematic biases of SNIa may propagate into the calibration results. Avoiding these biases might be important in light of the Hubble tension.

Looking for alternative calibrators becomes thus fundamental. In the future, the use of standard sirens up to $z \sim 4$ appears to be a promising route (Wang and Wang, 2019). As of now, data on galaxy clusters in the redshift range $0.14 \leq z \leq 0.89$ have, for instance, already been employed in the calibration of GRBs (Govindaraj and Desai, 2022). Moreover, Amati et al. (2019) recently introduced the use of Observational Hubble Data (OHD) to calibrate the Amati relation, something that has been further exploited using GP (Li et al., 2023; Kumar et al., 2023) and other techniques, such as the Bézier parametric curve obtained through the linear combination of Bernstein basis polynomials (Montiel et al., 2020; Luongo and Muccino, 2020, 2021, 2022). All these analyses aim to build an extended Hubble diagram through the calibration of GRBs, and then combine them with other data sets (e.g., SNIa, BAO) to study and constrain different cosmological models. There are several works related

to the application of the 3D Dainotti relation as a cosmological tool together with other probes (Dainotti et al., 2022a, 2023; Bargiacchi et al., 2023). In the last two papers, a discussion on the most appropriate likelihood assumptions must be made since while the Gaussian is the most appropriate assumption for GRBs it is not for the other probes including SNIa (Dainotti et al., 2024).

In this work, we aim to present a novel model-agnostic method to understand whether low-redshift calibrators can univocally determine the correlation parameters of GRBs, in order to use them as distance indicators. It is even more powerful than previous methods. In particular, we focus on the role played by the data on the Hubble function obtained from Cosmic Chronometers (CCH) (Jiménez and Loeb, 2002) in calibrating the Dainotti correlations using a specific data set of GRBs, called the Platinum sample. Recently, the 2D Dainotti relation has been calibrated with GP and OHD by Hu et al. (2021) and Wang et al. (2022), whose approach has been extended by Tian et al. (2023) also for the 3D relation. However, these authors adopt different OHD and GRB data sets from those considered by us in this work. Tian et al. (2023), in particular, use a combination of 31 $H(z)$ measurements from CCH and 5 from BAO data, after calibrating the latter assuming standard pre-recombination physics. The GRBs that they analyze are collected according to a different sample selection (radio plateau phases instead of X-ray plateau phases) and at different redshifts with respect to the Platinum sample. In addition, they do not take into account correlations between different CCH data points and, for the fitting analysis, they use a slightly different likelihood based on the D'Agostini method (D'Agostini, 2005). In our work, we employ the GP-reconstruction of the luminosity distance to calibrate the Dainotti relations, varying all the quantities that define the plane. We test the robustness of our results by selecting different priors on the parameters of the Dainotti relations and studying the impact of the covariance of the reconstructed luminosity distance. We do not use data on $H(z)$ from BAO to avoid the need to make model-dependent assumptions about the physics at the decoupling time in the calibration process. Moreover, we provide and justify a suitable set-up for the GP training and extend our methodology to account for the redshift-evolution corrections of the Dainotti relation, showing how this is actually of fundamental importance for the extension of the distance ladder.

This paper is organized as follows: in Sec. 2, we present and describe the two- and three-dimensional Dainotti relations, the latter defines the fundamental plane of GRBs; in Secs. 3 and 4, we describe the data sets and methodology employed in this work, respectively; in Sec. 5 we present our results, discussed in detail in Sec. 6. Finally, we draw our conclusions in Sec. 7.

2. The Dainotti correlations

The three-dimensional fundamental plane correlation, also known as 3D Dainotti correlation, reads (Dainotti et al., 2016, 2017a, 2020a)

$$\log L_{\rm X} = C_o + a \log T^*_{\rm X} + b \log L_{\rm peak}\,, \tag{1}$$

where

$$L_{\rm X} = 4\pi D_L^2 F_{\rm X} K_{\rm plateau} \tag{2}$$

is the X-ray source rest-frame luminosity,

$$L_{\rm peak} = 4\pi D_L^2 F_{\rm peak} K_{\rm prompt} \tag{3}$$

is the peak prompt luminosity (both luminosities are in units of erg s^{-1}) and $T^*_{\rm X}$ is the characteristic time scale which marks the end of the plateau emission (in units of s).[1] In the above equations, $F_{\rm X}$ is the measured X-ray energy flux at $T^*_{\rm X}$, $F_{\rm peak}$ is the measured gamma-ray energy flux at the peak of the prompt emission over a $1s$ interval (both fluxes are in units of erg cm^{-2} s^{-1}), $K_{\rm plateau} = (1+z)^{\alpha_{\rm plateau}-2}$ is the power-law plateau K-correction with $\alpha_{\rm plateau}$ being the X-ray photon index of the plateau phase. The K-correction for the prompt emission, $K_{\rm prompt}$, depends instead on the X-ray photon index ($\alpha_{\rm prompt}$), energy and differential spectrum. Only the GRBs for which the spectrum calculated at 1 second has a smaller χ^2 for a single power-law (PL) fit than for a cut-off power-law (CPL) are considered. In particular, following Sakamoto et al. (2011), when $\Delta\chi^2 = \chi^2_{\rm PL} - \chi^2_{\rm CPL} > 6$, the CPL model is preferred over the PL to compute $K_{\rm prompt}$ (see also Dainotti et al., 2016 for details).

The correlation parameters in Eq. (1) are identified by a, b, and C_o, where the a parameter denotes the anti-correlation between $\log L_X$ and $\log T^*_{\rm X}$ possibly driven by the magnetar (Rowlinson et al., 2014; Rea et al., 2015), b the relation between $\log L_{\rm peak}$ and $\log L_X$, and C_o is the normalization of the plane. When dealing with GRBs, one has also to consider that these data suffer from an unknown source of scatter on the plane, σ_{int}, which cannot be neglected since it specifies the tightness of the relation. This tightness relies on the spin period and magnetic field variations of a fast millisecond magnetar. Indeed, the plateau emission can be ascribed to the magnetar model (Dall'Osso et al., 2010; Rowlinson et al., 2014; Rea et al., 2015; Stratta et al., 2018), which describes that the X-ray plateaus are caused by a fast-spinning neutron star. In this case, the slope of the correlation, which is identified by a, is equal to -1. Other physically motivated interpretations have been discussed. For instance, in van Eerten (2014) it is shown that both $L_{\rm peak} - L_X$ and $L_X - T^\star_X$ correlation can be recovered within the standard forward shock model for GRB afterglows, with the addition of the microphysical parameters. We will see that our results are fully compatible with the magnetar model predictions.

While $T^*_{\rm X}, F_{\rm X}, \alpha_{\rm plateau}, F_{\rm peak}, \alpha_{\rm prompt}$ are measurable quantities, a, b, C_o, and σ_{int} can only be determined through a proper calibration, which requires the use of cosmological luminosity distances. It is immediate to notice in Eqs. (2) and (3) that both $L_{\rm X}$ and $L_{\rm peak}$ depend on the background cosmology since the luminosity distance D_L requires the knowledge of the functional form of the Hubble expansion rate. Assuming a flat Universe,[2]

$$D_L(z) = c(1+z)\int_0^z \frac{dz'}{H(z')}\,, \tag{4}$$

where the theoretical formulation of $H(z)$ is defined in Eq. (6). In this work, we leverage the availability of data on $H(z)$ from cosmic chronometers, which do not rely on very strong cosmological assumptions. We propose to use these measurements together with GP to reconstruct the shape of $H(z)$ and obtain agnostic estimates of the luminosity distance at the redshifts of the GRB data, $z_{\rm GRB}$.

As we will see later on, the model-independent analysis performed with the 3D Dainotti relation only sets an upper bound on the value of b, being our constraint on this parameter compatible with $b = 0$ at already 68% C.L. This is possibly pointing out that the contribution of the peak luminosity in the prompt emission is not needed for the use of the correlation as a viable cosmological tool, which reduces therefore to an X-ray time-luminosity relation, i.e. the *2D Dainotti correlation* (Dainotti et al., 2008). Neglecting b in Eq. (1), this relation is then defined as

[1] All the quantities appearing in the logs of Eq. (1) are made dimensionless, dividing them by their corresponding units.

[2] The TT, TE, EE CMB likelihood from *Planck* prefers a closed universe at the $\gtrsim 2\sigma$ level in the context of ΛCDM (Aghanim et al., 2020; Handley, 2021; Di Valentino et al., 2019). However, when data on BAO, SNIa, the full-shape galaxy power spectrum or CCH are also considered in the fitting analysis, the compatibility with spatial flatness (i.e., with $\Omega_k = 0$) is recovered (Aghanim et al., 2020; Efstathiou and Gratton, 2020; Vagnozzi et al., 2021a,b; de Cruz Pérez et al., 2023, 2024). Model-independent studies with low-z data reach also this conclusion, but with a larger uncertainty (Collett et al., 2019; Dhawan et al., 2021; Favale et al., 2023; Qi et al., 2023). See Di Valentino et al., 2021b for a review.

$$\log L_X = C_o + a \log T_X^* . \quad (5)$$

The 2D Dainotti relation rules out basic thin shell models but not the basic thick shell model (van Eerten, 2014). In the latter case, both forward- and reverse shock-dominated outflows are shown to be consistent with this relation. When a slope of -1.2 is observed, it means that accretion onto the black hole is favored, as discussed in Cannizzo and Gehrels (2009); Cannizzo et al. (2011).

We will apply our methodology to the calibration of both, the 3D and 2D Dainotti relations.

3. Data

In this section, we describe the data sets employed in this work.

3.1. The Platinum sample

Observations of 50 long GRBs (i.e., with a burst phase that lasts $> 2s$) in the redshift range $0.553 \leq z \leq 5.0$ constitute the so-called *Platinum sample*, defined for the first time in Dainotti et al. (2020a). It is a sub-sample of the larger Gold Sample (Dainotti et al., 2016). The Platinum sample collects well-defined morphological features of GRBs that show plateaus with an inclination $< 41°$ and that last $> 500s$ and with no flares. In terms of measured quantities at a given redshift z, we find five properties: $T_X^*, F_X, K_{\rm plateau}, F_{\rm peak}, K_{\rm prompt}$. These quantities can be related together to form a fundamental plane for the GRBs which finds its expression in the 3D Dainotti correlation in Eq. (1), or the 2D Dainotti correlation in Eq. (5) if one removes the contribution of the peak prompt luminosity. For details about the physical meaning of the GRBs properties and the correlations, we refer the reader to Sec. 2.

In Fig. 1, we present the 2D projection of the fundamental plane for both the full Platinum sample (50 GRBs) and the sub-set of 20 GRBs that fall within the redshift range covered by the CCH data, which are used in our calibration of the Dainotti relations (see Secs. 3.2 and 4, and Tables A.1 and A.2). Here we fix the parameters a, b, and C_o that enter the 3D relation to the values obtained from the fundamental plane fitting analysis. This is the standard procedure, widely used in the context of GRB cosmology. The likelihood is built by making use of the D'Agostini and Kelly method (D'Agostini, 2005; Kelly, 2007), and an underlying cosmological model is assumed to compute the luminosity distances entering Eqs. (2) and (3). An example of its application can be found in Dainotti et al. (2022b), where a flat ΛCDM model with $H_0 = 70$ km/s/Mpc is considered, while Ω_M is free to vary. We follow the same approach as in that reference in Fig. 1, just to visualize where the GRBs that constitute the Platinum sample are located in the plane according to the 3D Dainotti relation. The results obtained with 50 GRBs read $a = -0.88 \pm 0.12, b = 0.54 \pm 0.12, C_o = 23.04 \pm 6.23$ and $\sigma_{int} = 0.36 \pm 0.04$. For the results obtained with 20 GRBs, we refer instead the reader to the constraints listed in Table 1. We will use them later in the analysis to test the impact of the prior choice on the parameters themselves. As a last note, we add here that in order to check whether the sub-sample of 20 GRBs is representative of the full Platinum sample, we perform a Kolmogorov-Smirnov (KS) test (Kolmogorov, 1933; Smirnov, 1939) for all the variables of the Platinum sample used in this work, i.e. $\log T_X^\star$, $F_{\rm peak}$, $K_{\rm prompt}$, $\log F_X$ and $K_{\rm plateau}$. We also cross-check the results with the Anderson-Darling (AD) test (Anderson and Darling, 1952). These statistical analyses allow us to estimate the significance level for rejecting or not rejecting the null hypothesis that the two samples come from the same parent distribution. The results of both tests show that we cannot reject the null hypothesis at 95% C.L., as we find a p value greater than 0.05 in all the tested variables. This supports the choice of the GRBs sub-set used in the calibration analysis and this does not introduce any bias in this choice as no statistical difference in the sample is shown. We present the results of KS and AD tests in Appendix B.

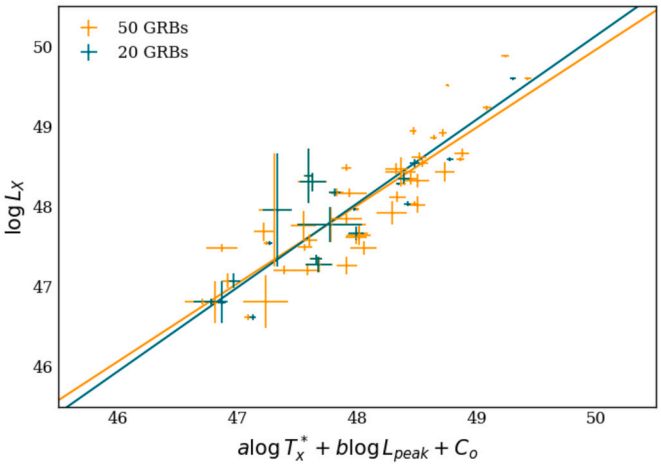

Fig. 1. 2D projections of the fundamental plane for the Platinum sample (in orange) and for the sub-sample of 20 GRBs used in this work (in green), both obtained taking the mean values of a, b, and C_o from the related fundamental plane fitting analyses. The error bars represent the 1σ uncertainty.

3.2. Cosmic chronometers

With the minimal assumption that the Universe is described by a Friedmann-Lemaître-Robertson-Walker metric, where the scale factor $a(t)$ is directly related to the redshift as $z = a^{-1} - 1$, the expansion rate of the universe can be written as follows

$$H(z) = \frac{\dot{a}}{a} = -\frac{1}{1+z}\frac{dz}{dt}, \quad (6)$$

that is, the Hubble function is related to the differential ageing of the universe dt as a function of z. However, the ratio dz/dt is not directly observable and one needs to identify objects in the Universe whose time evolution across redshift ranges can be accurately determined, i.e. *cosmic chronometers*. This can be done with the help of differential age techniques (Jiménez and Loeb, 2002). The best candidates for CCH are massive, passively evolving galaxies formed at $z \sim 2-3$ over a brief period, typically $t \sim 0.3$ Gyr. These galaxies are homogeneous over cosmic time, meaning that they have formed at the same time independently of the redshift at which they are observed. Indeed, they evolve on timescales much longer than their differential ages. This allows us to use the difference in their evolutionary states to reveal the time elapsed between the redshifts, i.e. how much time has passed since they have run out of their gas and stopped star formation. This is done assuming an underlying stellar population synthesis (SPS) model and analyzing their spectral energy distributions (SED). Indeed, while redshift measurements can be obtained with quite high accuracy through the spectral line analysis, the age is not directly observable and one has to adopt particular techniques such as photometry, single spectral regions (e.g. D4000 (Moresco et al., 2020)) or the full-spectral fitting. Within these galaxies, old stellar populations have minimal star formation rates and this ensures low contamination from young components. However, such measurements are not immune to systematics and various criteria have been considered to minimize contamination from factors like photometry, spectroscopy, stellar velocity and mass dispersion. Potential degeneracies between physical parameters of the galaxy SED (e.g., age-metallicity) also contribute to the error budget. The reconstruction of the star formation history of age-dating galaxies is very challenging. Nevertheless, a strength of CCH lies in estimating the quantity dt rather than the absolute age t. This approach minimizes the impact of systematic errors in absolute age estimation when measuring the differential age. All the possible sources of errors discussed above are taken into account in the covariance matrix provided by Moresco et al. (2020), which includes the contribution of both statistical and systematic errors, $C_{ij}^{\rm CCH} = C_{ij}^{\rm stat} + C_{ij}^{\rm sys}$. In particular, in addition to the statistical error,

the diagonal component of this matrix takes into account several systematics related to the estimate of the physical properties of a galaxy (e.g. stellar metallicity and the contamination by a younger stellar population), which are uncorrelated for objects at different redshifts. The non-null correlations arise from factors that instead rely on the common SPS model which, as explained above, is involved in studying the evolving galaxies. Beyond General Relativity and the assumption that standard physics applies in the environment of the galaxy stars, CCH are devoid of additional cosmological assumptions. For this reason, in the last years, they emerged as suitable candidates for model-independent analyses. They can be employed in the calibration of BAO and SNIa (Heavens et al., 2014; Verde et al., 2017; Yu et al., 2018; Gómez-Valent and Amendola, 2018; Haridasu et al., 2018; Gómez-Valent, 2022; Dinda, 2023; Favale et al., 2023; Mukherjee et al., 2024) or other objects like GRBs or QSOs (see, e.g., Amati et al., 2019; Montiel et al., 2020; Luongo and Muccino, 2021, 2022; Dinda, 2023; Kumar et al., 2023).

In this work, we use state-of-the-art data on CCH, constituted of 33 data points in the redshift range $0.07 < z < 1.965$, to calibrate the GRB Dainotti correlations. The complete list of CCH and the corresponding references can be found in Appendix A. The covariance matrix of the data is computed as explained in Moresco et al. (2020), using the codes provided in.[3]

4. Methodology

One can use measurements of the Hubble function to reconstruct the universe expansion history and solve the integral in Eq. (4) at the GRB redshifts. For this purpose, we employ GP. It is a machine learning tool that offers means of deriving cosmological functions through data-driven reconstructions under minimal model assumptions, keeping track of the correlations between them. Because of that, this algorithm has gained significant prominence in the context of model-agnostic regression techniques within the field of cosmology.

Being a generalization of a multivariate Gaussian, a Gaussian Process can be written by specifying its mean function $\bar{y}(z)$ and the covariance matrix $D(z,\tilde{z})$, i.e., $f(z) \sim \mathrm{GP}(\bar{y}(z), D(z,\tilde{z}))$ (Rasmussen and Williams, 2006). If we denote Z as the exact locations of the input data points, the covariance matrix D takes the following form

$$D(z,\tilde{z}) \equiv \begin{cases} K(z,\tilde{z}) + C(z,\tilde{z}) & \text{if } z \text{ and } \tilde{z} \in Z \\ K(z,\tilde{z}) & \text{otherwise} \end{cases}, \tag{7}$$

where C is the covariance matrix of the data and $K(z,\tilde{z})$ the kernel function. Indeed, although GP allow for agnostic (cosmology-independent) reconstructions, a specific kernel has to be chosen for the training. The latter is in charge of controlling the correlations between different points of the reconstructed function. Kernels depend on a set of hyperparameters, which follow a likelihood that is set by the probability of the GP to produce our data set at every point of the hyperparameter space. Before the reconstruction can take place, it is essential to determine the shape of this distribution. In many cases, this likelihood is sharply peaked and using the best-fit values of the hyperparameters becomes a good approximation (Seikel et al., 2012). However, from a Bayesian perspective, the correct approach involves obtaining the complete distribution of the hyperparameters to account for their correlations and propagate their uncertainties to the final reconstructed function (Gómez-Valent and Amendola, 2018; Hwang et al., 2023). This is the approach followed in this work.

From every set of hyperparameters drawn from the hyperparameter distribution one can construct the GP at the locations $Z^\star \neq Z$, which is characterized by the mean function

$$\bar{f}^\star = \bar{y}^\star + K(Z^\star, Z)[K(Z,Z) + C(Z,Z)]^{-1}(Y - \bar{y}) \tag{8}$$

and covariance matrix

$$\mathrm{cov}(f^\star) = K(Z^\star, Z^\star) - K(Z^\star, Z)[K(Z,Z) + C]^{-1} K(Z, Z^\star), \tag{9}$$

where Y are the data points located at Z and $\bar{y}^\star \equiv \bar{y}(Z^\star)$ is the a priori assumed mean of the reconstructed function at $Z^\star$. From this GP, one can then produce a sufficiently large sample of the function of interest at $Z^\star$ to ensure convergence.

In this work, we reconstruct $H(z)$ at the redshifts $z_{\rm GRB}(= Z^\star)$ of the $n_{\rm GRB} = 20$ GRBs of the Platinum sample that fall below the highest CCH redshift, $z = 1.965$, employing an a priori zero mean function, i.e. $\bar{H}(Z^\star) = 0$. The GRBs of our sub-sample lie therefore in the same redshift range of the calibrators. From the GP we obtain $N_{\rm real} = 5 \cdot 10^4$ realizations of $H(z)$ at each $Z^\star$ and the same number of luminosity distances, by solving the integral in Eq. (4). We ensure that the number of points in which we evaluate this integral is enough to have an accurate determination of the reconstructed function. This test is especially important in the region of redshifts below the GRB data point with the lowest redshift in our sample. To this purpose, we repeat the GP reconstruction of $H(z)$ by increasing the number of Z^* in $0 < z < 0.553$ and find that the resulting shape of $\log D_L(z)$ remains stable. Thus, we are allowed to use the result obtained at $Z^* = z_{\rm GRB}$ to calibrate the Dainotti relations, Eqs. (1) and (5). Indeed, combining Eq. (1) and (3) one can easily obtain the following quantity

$$\begin{aligned} \log D_L^{\rm th} =& a_1 \log T_{\rm X}^* + b_1(\log F_{\rm peak} + \log K_{\rm prompt}) + c_1 + \\ &+ d_1(\log F_{\rm X} + \log K_{\rm plateau}), \end{aligned} \tag{10}$$

which we denote as the theoretical value for the log-luminosity distance, with $D_L^{\rm th}$ written in units of cm. Here, $a_1 = a/2(1-b)$, $b_1 = b/2(1-b)$, $c_1 = ((b-1)\log(4\pi) + C_o)/(2(1-b))$ and $d_1 = -(1-b)/2$.

On the other hand, the GP+CCH result can be used to compute the logarithm of the luminosity distances, which we treat as our observed value, $\log D_L^{\rm obs}(z)$. We have checked that its distribution is Gaussian in very good approximation. The corresponding covariance matrix can be obtained as follows,

$$C_{\rm obs,ij} = \frac{1}{N_{\rm real}} \sum_{\mu=1}^{N_{\rm real}} (x_{\mu,i} - \bar{x}_i)(x_{\mu,j} - \bar{x}_j), \tag{11}$$

where $x_{\mu,i}$ is the value of $\log D_L^{\rm obs}(z)$ at the i-th redshift for each realization $\mu = 1, ..., N_{\rm real}$.

If we first consider uncorrelated errors, $\sigma_{\rm obs,i}$, i.e., if we consider a diagonal covariance matrix, we can build a chi-squared which takes the following form,

$$\chi^2(a,b,C_o,\sigma_{int}) = \sum_{i=1}^{N} \frac{[\log D_L^{\rm obs}(z_i) - \log D_L^{\rm th}(z_i,a,b,C_o)]^2}{(\sigma_{\rm obs,i}^2 + \sigma_{int}^2)}, \tag{12}$$

where $N = n_{\rm GRB}$. We sample the parameters of interest of the Dainotti relations a, b, C_o, and σ_{int} through a Monte Carlo Markov Chain (MCMC) analysis, making use of the `Python` public package `emcee`[4] (Foreman-Mackey et al., 2013), an implementation of the affine invariant MCMC ensemble sampler by Goodman and Weare (2010). The log-likelihood to be evaluated at each step of the Monte Carlo is

$$\begin{aligned} \ln\mathcal{L} &= -\frac{1}{2}\left[\sum_{i=1}^{N} \ln\{2\pi(\sigma_{\rm obs,i}^2 + \sigma_{int}^2)\} + \chi^2\right] = \\ &= -\frac{1}{2}\sum_{i=1}^{N} \ln\{2\pi(\sigma_{\rm obs,i}^2 + \sigma_{int}^2)\} - \\ &- \frac{1}{2}\sum_{i=1}^{N} \frac{[\log D_L^{\rm obs}(z_i) - \log D_L^{\rm th}(z_i,a,b,C_o)]^2}{\sigma_{\rm obs,i}^2 + \sigma_{int}^2}. \end{aligned} \tag{13}$$

[3] https://gitlab.com/mmoresco/CCcovariance.

[4] https://emcee.readthedocs.io/en/stable/.

In comparison to previous studies, we also allow the five parameters defining the fundamental plane ($\log T_X^*, F_{\rm peak}, K_{\rm prompt}, \log F_X, K_{\rm plateau}$, cf. Table A.1) to vary freely in the Monte Carlo. We treat them as nuisance parameters. These parameters are specific for each GRB. This means that, in the end, if we employ the 3D Dainotti relation (Eq. (1)) we have $5 \times n_{\rm GRB} = 100$ nuisance parameters. Of course, in the case of the 2D Dainotti relation (Eq. (5)), we only sample $\{\log T_X^*, \log F_X, K_{\rm plateau}\}$, so we deal with $3 \times n_{\rm GRB} = 60$ nuisance parameters. The posterior distribution is given by the product of the above likelihood and the Gaussian priors, and the constraints for the parameters of interest a, b, C_o, and σ_{int} are derived after performing the marginalization over the nuisance parameters.

Due to the high dimensionality of the problem, to ensure convergence we choose to use a sufficiently large number of walkers (~ 220 for the 3D relation and ~ 140 for the 2D one) as well as a large number of steps in the parameter space $n_{\rm steps} = 6 \cdot 10^5$. We make use of the `Python` package `GetDist` (Lewis, 2019) to obtain all the 1D posteriors and 2D contour plots shown in this paper, as well as the constraints for each parameter.

Given the novelty of our approach and in anticipation of future applications, in this work we evaluate the proposed methodology by assessing the impact of:

1. The prior choice in the Monte Carlo analyses. Given our aim to develop a method that is as model-independent as possible, we extensively test both Gaussian and flat priors to verify the robustness and compatibility of the results obtained with each.
   First, we use Gaussian priors on the parameters of interest a, b, C_o, and σ_{int}. To build the priors we use the mean values and the 1σ uncertainties from the fundamental plane fitting analysis for the X-ray Platinum sample with 20 GRBs (see Sec. 3.1). Their values are listed in Table 1. Then, we gradually increase the standard deviation of the Gaussian to 2-, 3- and 5σ, to reduce the informative imprint of the prior. Nonetheless, it is important to mention that to preserve the physical meaning of these parameters, we impose bounds on a, b and σ_{int}. In particular, imposing $a < 0$ ensures that there is an anti-correlation between L_X and T_X^* and when the value of a is close to -1 this implies that the energy reservoir of the plateau remains constant (see Sec. 2). However, we will show that this anti-correlation is indeed maintained regardless of the physical cut $a < 0$, as positive values of a are consistently distant from the region preferred by the data in all the calibration results presented in this work. Regarding the b parameter, we impose the prior $b > 0$, which is driven by observational evidence and theoretical predictions. A negative b is not physically supported, as it would mean that the higher the peak luminosity, the less bright the plateau. Indeed, as shown in, e.g., Dainotti et al. (2011b); Hascoet et al. (2014); Dainotti et al. (2015b, 2017a), there is observational evidence that the more kinetic energy there is in the prompt, the more is transferred in the afterglow phase. Thus, there is a positive correlation between L_X and $L_{\rm peak}$, which supports the choice of the prior. In addition, we will see that the use of this prior is also motivated by the strong degeneracy between b and C_0, which cannot be broken with current data within this model-independent approach. Imposing $b > 0$ allows us to break this degeneracy and thus avoid ending up in unphysical regions of the parameter space. Finally, the intrinsic scatter has to be greater than zero by definition. Lastly, we adopt flat priors on the parameters of interest, by transforming the previous Gaussian priors into uniform distributions. This conversion can be done in several ways and by applying different definitions. We decided to use the same approach employed by Dainotti et al. (2022a),[5] which requires

$$\mu = \frac{x_1 + x_2}{2}\,, \qquad \sigma = \sqrt{\frac{(x_2 - x_1)^2}{12}}\,. \tag{14}$$

   These are the relations to transform a Gaussian distribution with mean μ and standard deviation σ to a uniform distribution $\mathcal{U}(x_1, x_2)$ with the same mean and standard deviation.
2. The covariance matrix of the reconstructed function $\log D_L^{\rm obs}(z)$ at the GRB redshifts, $C_{\rm obs}$, as defined in Eq. (11). The total covariance matrix, $C_{\rm T}$, incorporates also the contribution of the intrinsic scatter $\sigma_{\rm int}$, which is the same for all the GRB data points. Its elements read $C_{\rm T,ij} = C_{\rm obs,ij} + \delta_{ij}\sigma_{int}^2$. Hence, if we define $\Delta_i \equiv \log D_L^{\rm obs}(z_i) - \log D_L^{\rm th}(z_i)$, generalizing Eq. (13), we can write the new log-likelihood

$$\ln \mathcal{L} = -\frac{N}{2}\ln(2\pi) - \frac{1}{2}\ln\det(C_{\rm T}) - \frac{1}{2}\sum_{i,j=1}^{N} \Delta_i^T (C_{\rm T}^{-1})_{ij} \Delta_j\,, \tag{15}$$

   which duly takes into account the correlations.

5. Results

In this section, we present the results of the calibration of the GRB correlation parameters with CCH. Specifically, in Sec. 5.1, we show how we can obtain the luminosity distance at the GRB redshifts without adopting any cosmological model, making use of the GP algorithm. Then, in Secs. 5.2 and 5.3, we use this result to perform the calibration of the 3D Dainotti correlation, without considering and considering the redshift evolution of the coefficients, respectively. These results lead us to study, in Sec. 5.4, the 2D Dainotti correlation, defined in terms of the X-ray time and luminosity at the end of the plateau emission. In all the aforementioned analyses, we investigate the impact of the prior choice on our results, drawing interesting conclusions about the calibrating role of the CCH, which we then discuss in detail in Sec. 6. In Sec. 5.5, we finally present the extension of the distance ladder obtained from the calibrated GRBs.

5.1. GRB luminosity distance from CCH and Gaussian processes

We first reconstruct the Hubble function using the CCH data and the associated covariance matrix described in Sec. 3.2, making use of the public package *Gaussian Processes in Python* (`GaPP`),[6] first developed by Seikel et al. (2012). We adopt the Matérn32 kernel and obtain the full distribution of its hyperparameters with `emcee`, as explained in Sec. 4. This is something that has not been done in previous works that employ the GP technique to calibrate GRB correlations (either with SNIa or CCH), and this is certainly important to properly compute the uncertainty of the reconstructed function. This also applies to the use of the CCH covariance matrix. Neglecting the CCH correlations in the GP reconstruction has a modest impact on the final shape of $H(z)$, as we have explicitly checked. The relative difference in units of σ between the correlated and uncorrelated CCH reconstructions is at most 15%, dropping at 1% in the data-poor region, for $z \gtrsim 1$ (with σ being the largest uncertainties of the two reconstructions, i.e. the CCH-correlated one). Regarding the selection of the kernel, in Favale et al. (2023), it is shown that different (stationary) kernels provide very similar results when the same CCH data set is used to reconstruct $H(z)$ and also that the most conservative choice is the Matérn32 covariance function, since it is the one that leads to the largest error budget, see the aforesaid reference for details. Supported by these previous results, we follow the same approach here. We reconstruct the Hubble function within the CCH data redshift range, i.e. $z \leq 1.96$. The resulting shape of $H(z)$ is shown in

[5] Therein the authors test the impact of the prior choice in a similar way but to infer cosmological parameters with SNIa and BAO.

[6] https://github.com/carlosandrepaes/GaPP.

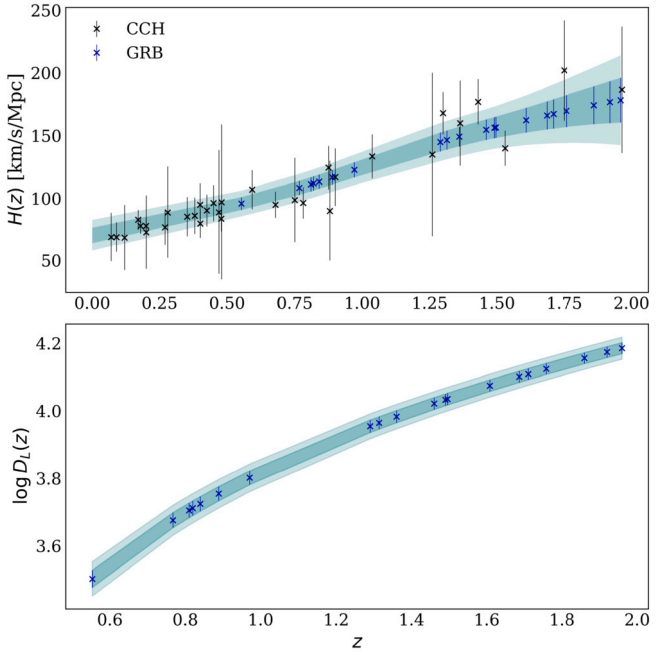

Fig. 2. *Top panel:* Reconstruction at 2σ C.L. of $H(z)$ with GP. We show the CCH data (in black) and the individual values of $H(z)$ at the various GRB redshifts (in blue), both at 1σ C.L. *Bottom panel:* The corresponding shape of $\log D_L(z)$. The argument of the log is made dimensionless by dividing the luminosity distance by 1 Mpc.

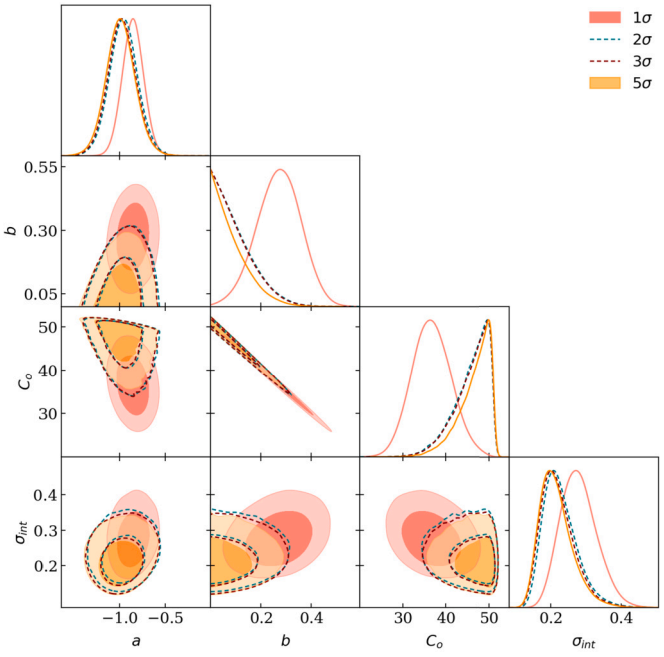

Fig. 3. 1D posteriors and 2D contours at 68% and 95% C.L. obtained in the analyses of the 3D Dainotti relation, assuming the n-σ progression for Gaussian priors and the physical cuts $a<0$, $b>0$, $\sigma_{int}>0$. Results obtained in the different cases are all consistent with each other. However, the 2σ, 3σ and 5σ priors are more conservative and allow for more model-independent results.

Table 1
Priors adopted for the 3D relation analysis. In the first column, we report the mean values and the corresponding 1σ uncertainties obtained from the GRB fundamental plane fitting (FP_{BF}) analysis, from which we take the Gaussian priors at n-σ. In the second and third columns, we list, respectively, the uniform prior ranges at 3- and 5σ C.L., computed using Eq. (14). We impose physical cuts on the parameters ($a<0$, $b>0$, $\sigma_{int}>0$). This is why some of the boundaries in the last two columns coincide.

	FP_{BF}	3σ	5σ
a	-0.81 ± 0.17	(-1.68, 0)	(-2.26, 0)
b	0.50 ± 0.17	(0, 1.37)	(0, 1.95)
C_o	24.65 ± 8.91	(-22,71)	(-53,102)
σ_{int}	0.35 ± 0.07	(0, 0.72)	(0, 0.97)

Fig. 2, together with the corresponding result for $D_L(z)$, obtained by using the GP-shapes of $H(z)$ and Eq. (4).

5.2. Calibration of the 3D Dainotti relation

Once obtained the reconstruction of $\log D_L^{\text{obs}}(z)$ together with its uncertainties, we can constrain the correlation parameters in Eq. (1) as well as the intrinsic scatter of the plane, by means of the likelihood in Eq. (13). As already mentioned in Sec. 4, to ensure the efficiency of the method and cross-check the stability of the results, we need to quantify the impact of the prior choice on the parameters of interest a, b, C_o, and σ_{int} in the Monte Carlo sampling. We thus employ Gaussian priors with a mean equal to that obtained in the fundamental plane (FP) fitting analysis and a standard deviation equal to 1, 2, 3 or 5 times the one obtained in the FP analysis (cf. Table 1). We present our results in Fig. 3. We then repeat the analysis making use of flat priors. We apply the conversion from Gaussian to flat priors of Eq. (14). However, in Table 1, we only report the results of this conversion for the 3- and 5σ cases since they lead to the most conservative results. We show the corresponding MCMC outcome in Fig. 4. Some conclusions follow:

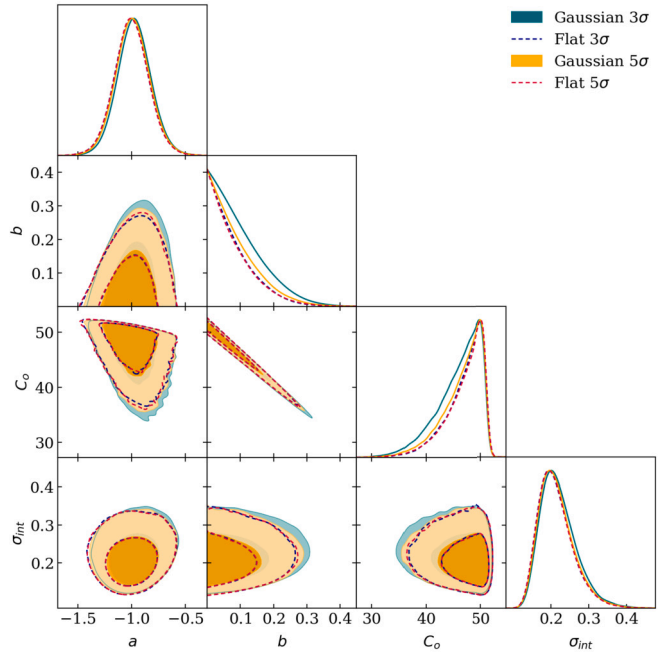

Fig. 4. 1D posteriors and 2D contour plots at 68% and 95% C.L. obtained in the analysis of the 3D Dainotti relation using Gaussian priors and the corresponding flat priors from Eq. (14) at 3- and 5σ. We use dashed lines for the results obtained with flat priors. They match almost perfectly with those obtained with Gaussian priors.

- Fig. 3 shows that results obtained with different Gaussian priors are all compatible with each other within errors. The largest differences are found with the 1σ prior. This difference can be easily understood. In the 1σ prior case, we only let the walkers explore a very limited region of the parameter space around the fundamental plane mean values.

Table 2
Constraints on the parameters of interest for the 3D and 2D Dainotti relations sampled assuming the baseline set-up, i.e. uniform priors at 5σ C.L., which leads to the most conservative results in this paper (see also Figs. 4 and 8). We report for each parameter the mode and mean value together with its associated uncertainty at 68% C.L., except for b, for which we give an upper bound at 95% C.L.

		a	b	C_o	$\sigma_{\rm int}$
3D relation	Mode values	-1.03	< 0.21	50.17	0.20
	Mean	-1.00 ± 0.16	< 0.21	$47.05^{+4.21}_{-1.35}$	$0.21^{+0.03}_{-0.05}$
2D relation	Mode values	-1.07		51.19	0.19
	Mean	-1.04 ± 0.16		51.16 ± 0.53	$0.21^{+0.03}_{-0.05}$

- Interestingly, as soon as we move away from the 1σ prior and the priors become less informative, the posteriors for a, b, C_o, and σ_{int} do not significantly change between different prior choices. This suggests that the method is stable. This is even more evident if we look at Fig. 4, which shows that passing from Gaussian to uniform priors does not alter the posteriors significantly. Given the stability of the results, hereafter, we will consider the set-up with flat priors at 5σ as our *baseline*, being this the most conservative choice. We report the mode and mean values of the one-dimensional marginalized distributions for each of the parameters of interest in Table 2.
- We find no preference for a non-zero value of b, suggesting that this parameter is not playing a major role in the evaluation of the cosmological results and hence we can use the 2D relation instead. Actually, its upper bound at 95% C.L. stands around 0.2 in all the analyses presented so far. From a Bayesian perspective, we are therefore motivated to consider the 2D Dainotti relation, given by Eq. (5). We will study this scenario in Sec. 5.4.
- There is a strong degeneracy between C_o and b. The one-dimensional posterior of the normalization factor exhibits a cut-off around $C_o \sim 52$, which is due to the aforementioned correlations and the physical bound $b > 0$ employed in our analysis of the 3D Dainotti relation (see Sec. 4). Indeed, in the 2D case we consistently find $C_o \sim 51$, since we are essentially saturating the prior by setting $b = 0$, cf. Sec. 5.4.

Finally, in order to quantify the impact of correlations between different redshifts in $\log D_L^{\rm obs}(z)$ obtained from GP+CCH, we perform an additional analysis in which we also include the contribution of the non-diagonal terms of the covariance matrix $C_{\rm obs}$ (Eq. (11)) by making use of the log-likelihood in Eq. (15). We compare the results obtained in this new analysis with those discussed above, obtained when we only consider a diagonal covariance matrix. Moreover, we also investigate the scenario in which we neglect the uncertainties of the reconstructed luminosity distances and only consider the effect of the intrinsic scatter, $C_{\rm T,ij} = \delta_{ij}\sigma_{int}^2$. The results are presented in Fig. 5, illustrating that the posteriors for the parameters a, b, C_o, and σ_{int} are insensitive to the GP+CCH uncertainties. In Sec. 6, we will provide two interpretations of this conclusion.

5.3. Calibration of the 3D Dainotti relation including redshift evolution corrections

To ensure the generality of our treatment, it is worth discussing the role of the corrections due to evolutionary effects. Indeed, each physical feature of the three-dimensional GRB fundamental plane, $L_{\rm X}$, $T_{\rm X}^*$ and $L_{\rm peak}$, is affected by selection biases due to instrumental thresholds and redshift evolution of the variables involved in the correlations. It is shown in (Dainotti et al., 2013a, 2015a,b, 2020a, 2022b,c) that in order to correct for these effects, one can employ the Efron & Petrosian method (Efron and Petrosian, 1992), which tests the statistical dependence among $L_{\rm X}$, $T_{\rm X}^*$ and $L_{\rm peak}$. For details, see also Dainotti et al. (2017b, 2022a). Once one introduces this correction, the expression for the GRB fundamental plane takes the following form:

$$\begin{aligned}\log L_{\rm X} - k_{L_x}\log(1+z) =& a_{ev}(\log T_{\rm X}^* - k_{T_{\rm X}^*}\log(1+z)) + \\ &+ b_{ev}(\log L_{\rm peak} - k_{L_{\rm peak}}\log(1+z)) + \\ &+ C_{o,ev}\,. \end{aligned} \tag{16}$$

The subscript *ev* is employed here to distinguish the relation parameters from those employed in the non-evolutionary case, while $k_{L_x}, k_{T_{\rm X}^*}$ and $k_{L_{\rm peak}}$ represent the evolutionary coefficients related to each physical feature.

Starting from Eq. (16), one can derive the new likelihood, which now accounts for redshift evolution effects, thus assessing how they can affect the correlation parameters. We evaluate the impact of flat priors on $a_{ev}, b_{ev}, C_{o,ev}, \sigma_{int,ev}$ but only at 3- and 5σ, motivated by our previous results. To use the transformation in Eq. (14), we started from the results obtained from the analysis of the Platinum sample presented in (Dainotti et al., 2022a), which, at 1σ, read: $a_{ev} = -0.85 \pm 0.12$, $b_{ev} = 0.49 \pm 0.13$, $C_{o,ev} = 25.4 \pm 6.9$, and $\sigma_{\rm int,ev} = 0.18 \pm 0.09$. For the evolutionary coefficients entering Eq. (16), we take advantage of two results obtained for

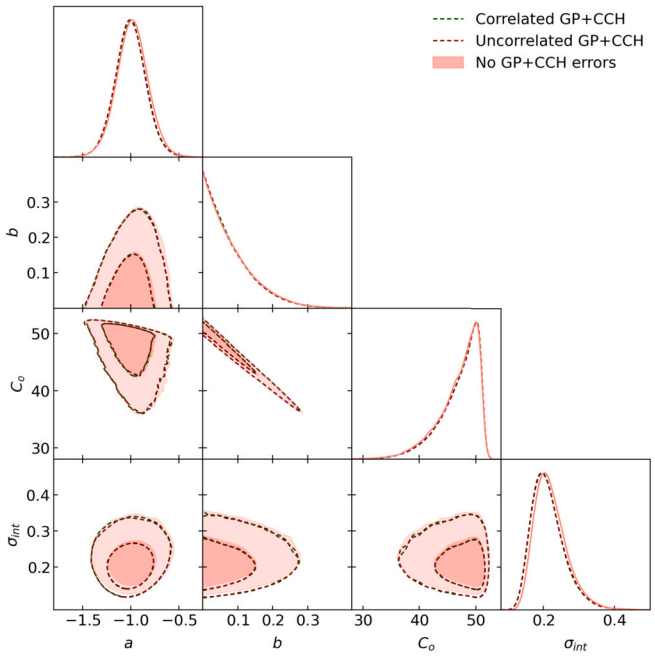

Fig. 5. 1D posteriors and 2D contour plots at 68% and 95% C.L. for the parameters of the 3D Dainotti relation, obtained assuming flat priors at 5σ. We study the impact of accounting for correlations between redshifts in the luminosity distance estimates reconstructed with GP+CCH (dotted green), neglecting those correlations (dotted red) and completely ignoring the uncertainties in the reconstruction (in pink). Differences are derisory.

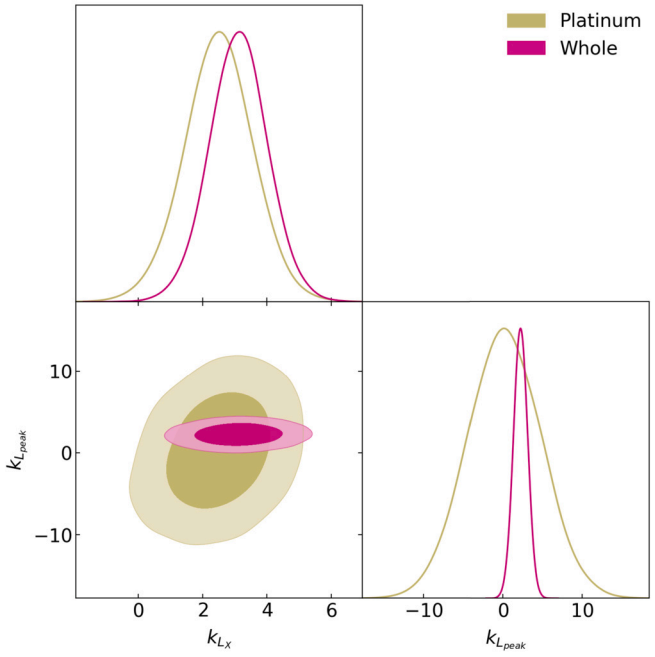

Fig. 6. 1D posteriors and 2D contour plots at 68% and 95% C.L. for the evolutionary coefficients k_{L_X} and $k_{L_{peak}}$, sampled assuming Gaussian priors at 3σ C.L. from the Platinum sample (in green) or from the Whole sample (in magenta). For the parameters $a_{ev}, b_{ev}, C_{o,ev}$ (not shown here) we impose flat priors at 5σ, cf. the main text and Fig. 7 for details.

the full Platinum sample (50 GRBs) and also for the Whole sample (222 GRBs) in (Dainotti et al., 2022a). At 68% C.L. they read, respectively:

$$\begin{aligned} &k_{L_x} = 1.37^{+0.83}_{-0.93}, \quad k_{T^*_X} = -0.68^{+0.54}_{-0.82}, \quad k_{L_{\rm peak}} = 0.44^{+1.37}_{-1.76}, \\ &k_{L_x} = 2.42^{+0.41}_{-0.74}, \quad k_{T^*_X} = -1.25^{+0.28}_{-0.27}, \quad k_{L_{\rm peak}} = 2.24 \pm 0.30\,. \end{aligned} \tag{17}$$

The above constraints are obtained assuming a flat ΛCDM model. We decide to proceed in two ways:

- Keep them fixed (Case 1);
- Let them vary in the Monte Carlo analysis, treating them as nuisance parameters (Case 2).

In Case 1), we just fix the k's to the central values reported above. In Case 2), we also use their uncertainties to build the corresponding priors. This is equivalent to propagating them to the parameters of interest in the MCMC analysis. This additional case is indeed performed to coherently reduce the model dependency level with this work's investigation line. Notice, though, that since $k_{T^*_X}$ does not depend on cosmology (being related to a measure of a characteristic time scale for the end of the plateau emission), we keep it fixed while we treat as nuisance parameters k_{L_X} and $k_{L_{\rm peak}}$. Since, as one can appreciate from Eq. (17), the Platinum constraints already come with large errors due to the small sample size and a large number of parameters, we decide to set Gaussian priors (instead of uniform priors) at 3σ on both k_{L_X} and $k_{L_{\rm peak}}$ to avoid non-physical results for these parameters. We also tested what happens if we consider uniform priors at 3σ. We have checked that the results for a_{ev}, b_{ev}, and $C_{o,ev}$ are not affected by this choice.

In Fig. 6, we show the corresponding posteriors of the evolutionary coefficients. At 68% C.L., we obtain $k_{L_X} = 2.50^{+1.06}_{-1.05}$ and $k_{L_{\rm peak}} = 0.20^{+4.67}_{-4.66}$ when we employ priors from the Platinum sample, while we find $k_{L_X} = 3.12 \pm 0.90$ and $k_{L_{\rm peak}} = 2.23 \pm 0.89$ from the Whole sample. As expected, the uncertainties for the latter case are smaller since the fundamental plane fitting analysis for the Whole sample has more constraining power (see Eq. (17)), being the data set larger. We here notice

Table 3
Priors adopted for the 2D relation analysis. The first column reports the mean values and the corresponding 1σ uncertainties obtained from the GRB fundamental plane fitting analysis. In the next two columns, we report uniform prior ranges at 3- and 5σ C.L., respectively, computed from Eq. (14).

	$\rm FP_{BF}$	3σ	5σ
a	-1.03 ± 0.16	(-1.85, -0.2)	(-2.39, 0)
C_o	51.2 ± 0.52	(48, 54)	(47,56)
σ_{int}	0.43 ± 0.08	(0.01, 0.85)	(0, 1.13)

that from our analysis, similarly to the analysis performed by Dainotti et al. (2022a) the parameters of the evolution are compatible within 1σ for both $k_{L_X}, k_{L_{\rm peak}}$ showing the reliability of this analysis as well. For what concerns the parameters of interest, we prefer to show their constraints in a whisker plot in Fig. 7, to compare the results throughout all the different cases described above (i.e., Cases 1 and 2, and considering no evolution), using flat priors at 5σ C.L.[7] It is remarkable to notice, again, that different settings provide very stable results on the correlation parameters, even when redshift evolution corrections are accounted for. Additionally, despite very small differences, all the scenarios lead to a tight relation, especially when the k's vary freely. Indeed, in this case we find $\sigma_{int} = 0.20^{+0.03}_{-0.05}$ instead of $\sigma_{int} = 0.22^{+0.03}_{-0.05}$ (with mode values 0.18 instead of 0.20, respectively). If we consider that σ_{int} is a measure of the scatter, which can depend on the spin period and magnetic field variability in each GRB, values so close to each other mean that the system has similar values of these parameters, with small variations.

5.4. Calibration of the 2D Dainotti relation

As seen in Secs. 5.2 and 5.3, the CCH calibration leads to a result for b that is compatible with 0 at 68% C.L. Thus, it is worth analyzing the 2D relation, which incorporates the properties of the end time of the plateau emission and the X-ray luminosity. The parameters to sample are, in this case, a, C_o, and $\sigma_{\rm int}$. Starting from Eq. (5), the same reasoning used to obtain the log-luminosity distance in Eq. (10) applies here, where we drop the contribution of $\log L_{\rm peak}$. It is straightforward to see that Eq. (10) reduces to

$$\log D_L^{\rm th} = a_1 \log T^*_{\rm X} + c_1 + d_1(\log F_{\rm X} + \log K_{\rm plateau})\,, \tag{18}$$

where now $a_1 = a/2$, $c_1 = (-\log(4\pi) + C_o)/2$ and $d_1 = -1/2$. On the same line of Sec. 5.2, we assess the impact of the different priors in the MCMC analysis. Their values are listed in Table 3 while the MCMC results are shown in Fig. 8.

We report both the mode values and the means of the one-dimensional marginalized distributions in Table 2. The constraint we obtain for a resonates well with the expectations: a slope of ≈ -1 implies a constant energy reservoir during the plateau phase (Dainotti et al., 2013a; Stratta et al., 2018). In particular, we can ascribe this phase to energy injection by newly born neutron stars (Dai and Lu, 1998; Zhang and Meszaros, 2001), and this result supports that the rotational energy of the latter is constant, indicating that they can be treated as a standard candle (Wang et al., 2022). Here, however, we clarify that the construction of the Platinum sample starts from phenomenological choices of the flatness of the plateau, the absence of flares, etc. and therefore, in our approach, we can independently obtain the magnetar-driven parameters. Indeed, the a slope is independent of the initial priors.

[7] We have also tested the case with uniform priors at 3σ on $a_{ev}, b_{ev}, C_{o,ev}, \sigma_{int,ev}$. However, for a specific set of k's (Whole or Platinum), the posteriors from 3- or 5σ do not change. Therefore, we prefer to show only the comparison between the analyses for a specific prior range choice (in this case, 5σ).

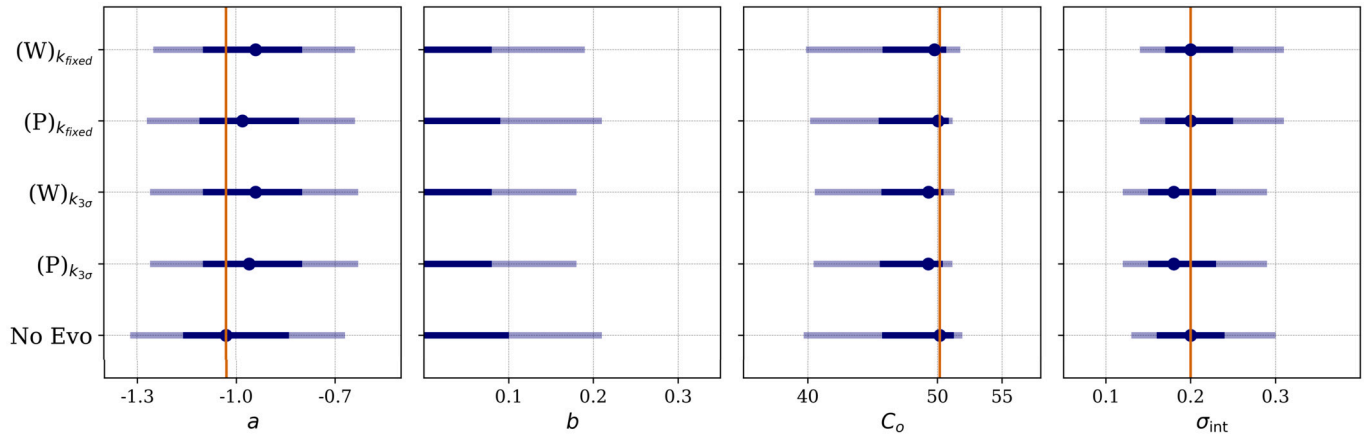

Fig. 7. Whisker plot for the parameters of interest evaluated at 68% and 95% C.L. (for b we only show its upper bounds), with the dots indicating the mode values of the one-dimensional marginalized distributions. The orange line passes through the *No Evo* (no evolution) mode values, obtained from the analysis with flat priors at 5σ in Sec. 5.2. With W we denote the results obtained considering the evolutionary coefficients from the Whole sample, the Platinum is instead indicated with P. The label k_{fixed} refers to the analyses in which the k's are fixed, whereas $k_{3\sigma}$ refers to those analyses in which the k's are allowed to vary within 3σ. For details, we refer the reader to the main text in Sec. 5.3. In the cases with evolution, a, b, C_o, σ_{int} become, respectively, $a_{ev}, b_{ev}, C_{o,ev}, \sigma_{int,ev}$.

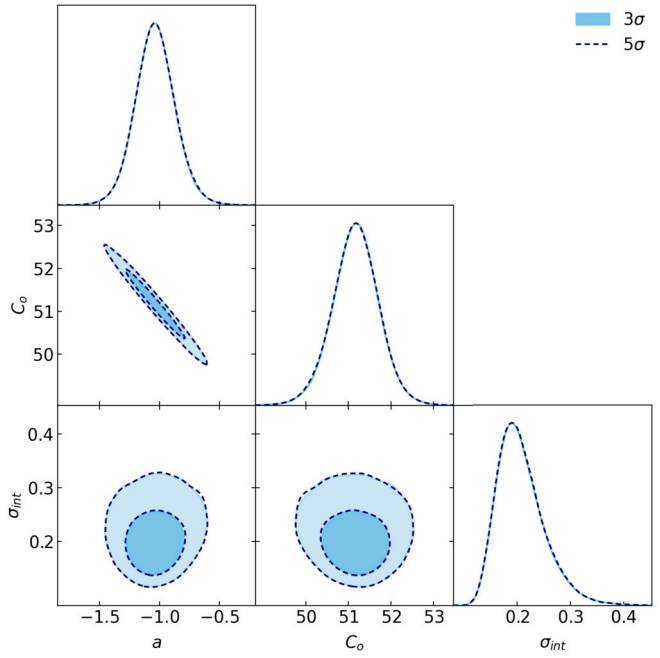

Fig. 8. 1D posteriors and 2D contour plots at 68% and 95% C.L. from the MCMC carried out for the 2D Dainotti relation assuming flat priors at 3- and 5σ, in cyan and blue, respectively. The results match each other, showing also in the case of the 2D relation the insensitivity of the analysis to the prior choice.

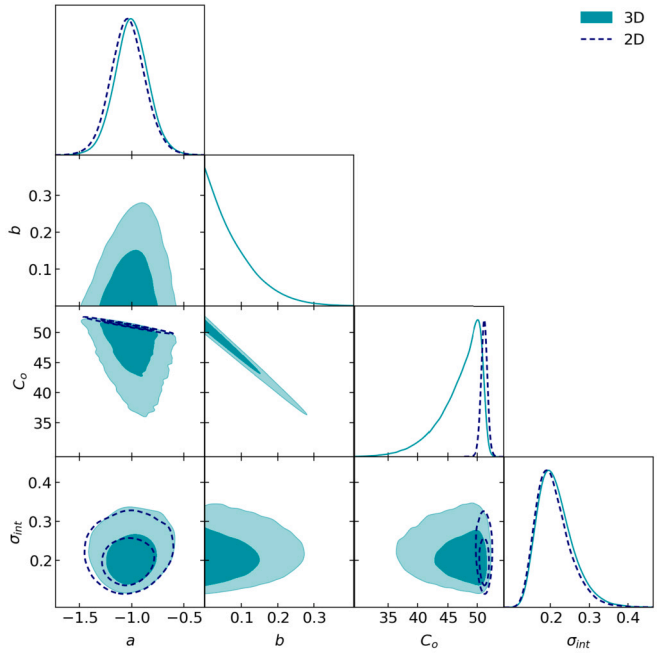

Fig. 9. Comparison between the MCMC results for the 3D and 2D Dainotti relations obtained with the baseline set-up in Secs. 5.2 and 5.4, respectively.

In the 2D Dainotti relation, we essentially set $b = 0$, so we break the strong degeneracy between this parameter and C_o (see Sec. 5.2 and Fig. 9). This explains why the uncertainty on C_o decreases by 80% compared to the baseline constraint obtained in Sec. 5.2. This fact may enhance our ability to constrain cosmology.

Finally, we assess the impact of the correlations in the values of $\log D_L^{\rm obs}$ obtained from the GP reconstruction by applying to the 2D relation the procedure explained at the end of Sec. 5.2. We find that our conclusions remain valid within this framework as well.

5.5. The extension of the distance ladder with and without evolution

Supported by the stability of the results achieved in the previous sections, it becomes natural to ask how such results can be leveraged in cosmological applications. As already mentioned, the advantage of using probes such as GRBs lies in their ability to extend the ladder beyond SNIa and BAO redshifts. This is the reason why we now employ the calibration results obtained making use of the GRB data at $z \lesssim 2$ to obtain luminosity distances from the remaining GRBs contained in the Platinum sample and cover the region up to $z = 5$ (we refer the reader to Table A1 of Cao et al. (2022a) for these additional GRBs data). We first check that the correlation coefficients between the calibration and nuisance parameters of the 20 GRBs involved in the calibration process are negligible and also that the posterior distributions of the nuisance parameters are highly in accordance with the corresponding prior distributions. Indeed, we find that the posterior and prior distributions are almost indistinguishable, with only a couple of exceptions (one nuisance parameter in two out of the 20 redshift points) in which we find noticeable changes, which remain in any case small ($\lesssim 1.9\sigma$). This allows us to sample the nuisance parameters of the GRBs at $z > 2$ together with the nuisance and calibration parameters of those GRBs at $z < 2$ to finally

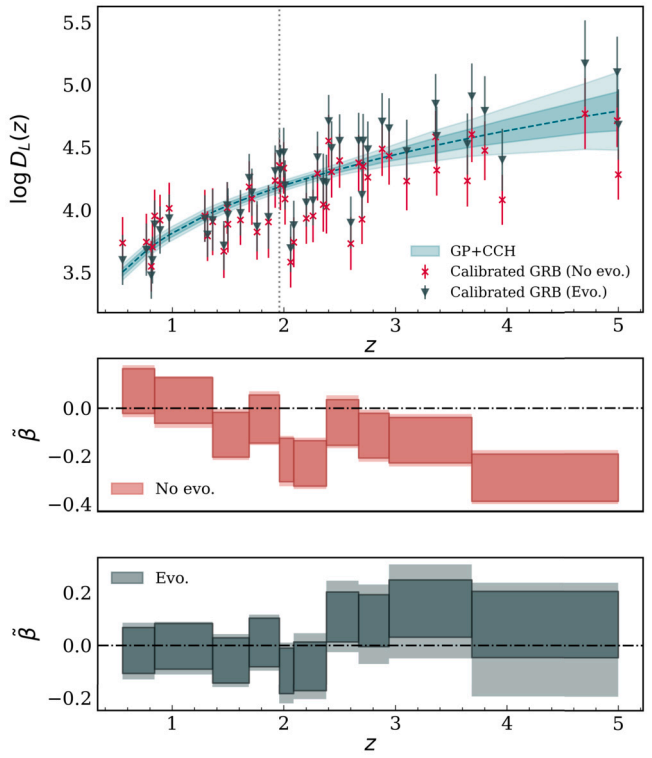

Fig. 10. *Upper plot*: The extended distance ladder. The GP+CCH reconstruction of the logarithm of the luminosity distance as a function of the redshift is shown in light green. The calibrated GRB data obtained with and without evolution effects are presented in gray and light red, respectively. The dotted vertical line at $z = 2$ is used to mark the border between the data employed in the calibration process and those used only in the extension of the ladder. The error bars of the calibrated GRB distances stand at 1σ C.L., while for the GP result we show both the 1σ and 2σ bands. The luminosity distance is given in Mpc; *Middle plot*: Weighted mean of the bias between the GP+CCH reconstruction and the calibrated GRB data with its uncertainty, as given in Eq. (19), when the evolution effects are neglected. Lighter-colored boxes are obtained when correlations are accounted for, see Sec. 5.5 for details; *Bottom plot*: The same as in the middle plot, but considering the evolution effects.

obtain the luminosity distances and build the extended distance ladder. In this way, we make sure to propagate the errors from the MCMC analysis to the final result. In particular, on top of these errors, we add the contribution of the intrinsic scatter to obtain the final uncertainties on the GRB luminosity distances.

In the upper plot of Fig. 10, we present the extended distance ladder obtained with our *baseline* calibration without considering evolution effects and compare it with the one obtained when the latter are also taken into account. In particular, for the latter, we employ the results obtained when the evolutionary coefficients, k_{L_X} and $k_{L_{peak}}$, are left free to vary according to the priors from the Whole sample since they lead to the tightest results and the smallest σ_{int} for the Dainotti relations (see Sec. 5.3). To quantify possible deviations from the GP+CCH distances, for each calibration result, we compute the bias between their mean and the mean of the GP+CCH reconstruction at each redshift, $\beta = \log D_L^{\rm GRB} - \log D_L^{\rm GP+CCH}$. In the calibrated GRB data points of $\log D_L(z)$ obtained without evolution effects, displayed in the upper plot of Fig. 10, one can already see a trend towards negative values of β in the region $z > 2$. The latter behavior was already found in previous works; see, e.g., Postnikov et al. (2014). To keep track of this trend in a more precise way, we compute a binned bias. More concretely, we opt to bin the redshift range, composed of 50 points, in 10 equi-populated redshift bins. In order to account for the existing correlations between the various data points in each bin, we compute the weighted mean and its uncertainty as follows:

$$\tilde{\beta}_k = \frac{\sum_{i,j=e_k}^{f_k} \beta_i \omega_{ij}}{\sum_{i,j=e_k}^{f_k} \omega_{ij}}, \tilde{\sigma}_k = \sqrt{\frac{1}{\sum_{i,j=e_k}^{f_k} \omega_{ij}}}, \tag{19}$$

with $\omega_{ij} = (C^{-1})_{ij}$ the elements of the inverse of the covariance matrix of the GRB luminosity distances, $e_k = 1 + 5(k-1)$, and $f_k = 5k$. This is an accurate computation since the distribution of the GRB luminosity distances is Gaussian in very good approximation, as we have explicitly checked and in accordance with a recent work of Dainotti et al. (2023). We present our results in the middle and bottom panels of Fig. 10, neglecting and considering the evolution corrections, respectively. In each of these two plots, we also show the weighted bias obtained when we neglect the off-diagonal terms of C. By comparing the middle and bottom plots, one can see that accounting for redshift evolution corrections is very important to decrease the bias in the region $z > 2$. In fact, when no evolution effects are considered, there is a clear trend towards smaller luminosity distances, as already noted in the upper plot of Fig. 10. We show now that correcting for evolutionary effects enables us to cure this trend, and this is even more true when we consider the existing correlations between the various GRB luminosity distances. Indeed, it is a well-known result that the physical properties of astrophysical objects at high z are more affected by the Malmquist bias (Malmquist, 1922) due to the difficulty of observing faint events at larger distances. This proves that if one wants to exploit probes at higher z for cosmological purposes, it is of utmost importance to use correlations in which possible biases and effects of redshift evolution have been properly evaluated and corrected.

6. Discussion

All the analyses presented in Secs. 5.2-5.4 share a common result. Our method is stable under the choice of the priors on the parameters that characterize the plane a, b, C_o, σ_{int}. Even when using Gaussian priors at 1σ, the posteriors on the parameters are compatible within $\sim 1-2\sigma$ to the other cases with wider priors. The differences between all the cases analyzed are very small, although we achieve the tightest constraints for the 3D relation parameters when flat priors at 5σ are employed (see for clarity Fig. 4). In addition, we find that the contribution of the peak luminosity in the prompt emission to the 3D Dainotti relation is not particularly favored from a Bayesian perspective, but cannot be excluded either. Our results only set an upper bound on b. More specifically, we find that $b \lesssim 0.2$ at 95% C.L. This result differs from what has been previously derived in analyses in which, to avoid the circularity problem, the parameters of the correlations are varied together with the cosmological parameters in a simultaneous fitting. In that case, the 3D relation is strongly preferred over the 2D one. This preference is supported by the analysis in (Cao et al., 2022a), which considers six different flat and non-flat dark energy models and different GRBs data sets, which also include the full Platinum sample. However, our findings are not only fully independent of cosmological models but are also in agreement with theoretical predictions and reach a level of accuracy suitable for constraining cosmological parameters (see, in particular, the results in Sec. 5.4). Since we find b to be compatible with 0 at 68% C.L. when we employ priors at 3 and 5σ, we feel motivated to also study the 2D relation in this work.

The baseline calibration both for the 2D and 3D Dainotti relations leads to an intrinsic scatter of the order of ≈ 0.2 with a relative precision of $\sim 20\%$. Specifically, for the 3D relation we obtain $\sigma_{int} = 0.21^{+0.03}_{-0.05}$. If compared with standard analyses, such as the fundamental plane fitting result with the same number of GRBs (see Table 1), we obtain a decrease of $\sim 40\%$ in its central value, outlining the achievement of a tighter relation. In particular, we can also quantify the compatibility of the two aforementioned results by calculating the relative difference of $\sigma_{int,\rm FP}$ compared to σ_{int} normalized by the maximum of the two uncertainties which reads as: $(\sigma_{int,\rm FP} - \sigma_{int})/\delta$, with $\delta = \max(\delta_{\sigma_{int}}, \delta_{\sigma_{int,\rm FP}})$. We find it to be 1.99, showing that the calibration result is consistent within 2σ with the standard (model-dependent) analysis results. As a term of

comparison, employing a different OHD data set and thus a different set of 23 GRBs, Tian et al. (2023) calibrate the 3D Dainotti relation with the D'Agostini method and obtain a very large scatter, $\sigma_{int} = 0.70 \pm 0.10$. In general, a lower dispersion is expected when GRBs are employed closer to the plane. One example can be found in (Dainotti et al., 2022b), where the 10 GRBs closest to the plane are selected from the Platinum sample, leading to $\sigma_{int} = 0.05 \pm 0.05$ (assuming a flat ΛCDM model). This analysis has the scope to show how many of these GRBs should be used in the future once more data is available in order to achieve the same precision of the SNIa standard candles in constraining cosmological parameters. In this regard, we can ask ourselves what impact the intrinsic scatter of the GRBs has on the calibration with CCH. At the end of Sec. 5.2, we actually perform an analysis to answer this question. Indeed, we have seen that our results remain unchanged whether or not we include the uncertainties on the reconstruction of the luminosity distance in the likelihood. This result holds for both the 2D and 3D relations and has two main implications. First, it confirms even more the stability of all the results obtained throughout this work. It establishes the CCH as a reliable calibrator for pinpointing a specific GRB sub-set with low intrinsic scatter. This is remarkable if one considers that this result holds even when the redshift evolution corrections are accounted for, thus making the relation and the results themselves more robust if also compared with previous results in the literature. Indeed, we obtain a mode value for σ_{int} which stands between 0.18 and 0.20, the lowest being obtained when also the evolutionary coefficients are left free in the analysis. As a comparison, Dainotti et al. (2022c) find $\sigma_{int} = 0.22 \pm 0.10$, and most recently this value has been better constrained in (Dainotti et al., 2022a), where they find $\sigma_{int} = 0.18 \pm 0.07$. Both results are obtained using the full Platinum sample and assuming a flat ΛCDM model. When we compare the uncertainty on this latter result including the correction for evolution, $\delta_{\sigma_{int}} = 0.07$, with our result, $\delta_{\sigma_{int}} = 0.04$, we obtain a decrease of 43%. This result makes this method competitive with standard approaches, especially for using GRBs for cosmological purposes in light of the already discussed circularity problem. Additionally, there is still a non-negligible dispersion on the GRB plane compared to other probes. As it stands, this dispersion is sufficiently large to prevent a better calibration regardless of the potential increase in the amount of CCH data at $z \lesssim 2$ through dedicated galaxy surveys in the future (see, e.g., Moresco et al. (2022)).

Fig. 10 is exactly telling us that, although GRB data alone cannot achieve yet the same constraining power as other low-redshift probes (see the difference in the error bars with respect to GP+CCH at the lowest redshifts), their strength lies precisely in their capability of extending the ladder to higher redshifts. We remark here that this has motivated in the last two decades the effort to build several correlations that can be used in this context, provided that understanding of their physical meaning and reliability regardless of selection biases do hold. However, these two aspects have not yet been fully addressed in many of the correlations. These correlations have been similarly calibrated with low-z anchors, and their intrinsic scatter ranges from $\sim$ 0.2 to 0.55. For instance, the Amati relation has been widely calibrated with SNIa using GP or simultaneous fitting analyses. The former approach was followed, for example, by Liu et al. (2022) and Liang et al. (2022), who found an intrinsic scatter between 0.46 and 0.52. The last authors further conducted simultaneous fitting with 31 OHD within the ΛCDM and wCDM models, yielding central values ranging from 0.39 to 0.46, depending on whether the A220 or A118 sample is used (Khadka et al., 2021). Kumar et al. (2023) calibrated the Amati relation using GP and 32 CCH, along with the A220. They determined the scatter to be $0.289^{+0.015}_{-0.014}$. To mention a few others, Li et al. (2023) used SNIa with GP in the A118 GRB sample at redshift less than 1.4, finding central values of 0.49 to 0.55, depending on the likelihood employed, whereas Mu et al. (2023) obtained a dispersion of 0.54 with SNIa in conjunction with the A220 sample. Alfano et al. (2024) found a scatter around 0.36 employing a simultaneous fitting for the Yonetoku relation. In light of these mentioned results, it is evident that a common low dispersion is not still reached for relations based solely on the prompt emission phase. The result achieved in this work represents so far, and at the best of our knowledge, one of the tightest correlations present in the literature. One possible explanation could be related to the fact that the plateau phase is less varied in its intrinsic properties with respect to the prompt emission. The scatter we find is robust to corrections for selection biases and redshift evolution, in contrast with other correlations, in which these effects still play a non-negligible role. If these corrections significantly affect the correlations, the correlations will no longer exist intrinsically in a reliable way. Also, the physical explanation of a relation meant to be used as a standard candle should be clear. For the correlations analyzed in this work, the most accredited theoretical scenario is the magnetar emission, and we actually found our results to support this model as the slope of the correlation is compatible with -1. These aspects make the extended ladder, which can be regarded as the final product of this calibration, even more robust and powerful to be employed in future cosmological applications.

7. Summary and conclusions

In this work, we have calibrated the Dainotti relations through a model-independent method that makes use of cosmic chronometers as calibrators. Thanks to the stability of our results across all the analyses presented, we can conclude that these low-redshift data are capable of identifying a valuable set of standardizable candles. Indeed, through the CCH calibration, the 20 GRBs we analyzed in $0.553 \leq z \leq 1.96$ are found to adhere tightly to the fundamental plane. In particular, we achieved one of the lowest levels of intrinsic scatter observed to date, and we derived constraints on the 2D and 3D Dainotti relations. These constraints are compatible with the physics of the relation itself, thus supporting, even more, its theoretical interpretation. This set can, therefore, be a promising candidate for future use in cosmological applications, as we have already demonstrated in this work by extending the distance ladder up to $z = 5$ through an unbiased GRB correlation.

Finding novel distance indicators that can be both less affected by biases and systematics and capable of extending the range of applicability of the cosmic distance ladder method to larger redshifts has become an important challenge in cosmology and astrophysics. However, if we aim to obtain unbiased cosmological distances, the calibration procedure cannot be subject to strong model-dependent assumptions. This is particularly relevant in light of the existing cosmological tensions, such as the one on H_0. This prospect further motivates ongoing efforts to achieve increasingly precise measurements, enhancing the statistics at low redshifts and in regions where objects like GRBs or QSOs can be crucial. On the other hand, the spread in the GRBs observed luminosities is still a non-negligible issue due to the not yet well-defined nature of their origin (core collapse of a massive star, merger of two neutron stars in a binary system or a neutron star-black hole system merger). Therefore, it becomes essential to investigate the reliability of these alternative probes and the relations that govern their intrinsic properties, possibly taking advantage also of the improvement both in data quality and quantity with upcoming surveys, e.g., SVOM (Atteia et al., 2022) or THESEUS (Amati et al., 2021) missions. In this way, model-independent calibration methods could play a significant role in standardizing these probes effectively, thereby further extending the cosmic distance ladder and broadening our ability to probe the fundamental cosmological parameters.

CRediT authorship contribution statement

Arianna Favale: Writing – original draft, Project administration, Methodology, Formal analysis, Conceptualization. **Maria Giovanna Dainotti:** Writing – review & editing, Methodology, Data curation, Formal analysis, Conceptualization. **Adrià Gómez-Valent:** Writing – review & editing, Supervision, Methodology, Formal analysis, Conceptu-

alization. **Marina Migliaccio:** Writing – review & editing, Supervision, Methodology, Formal analysis, Conceptualization.

Declaration of competing interest

The authors declare that they have no known competing financial interests or personal relationships that could have appeared to influence the work reported in this paper.

Acknowledgments

AF and MM acknowledge support from the INFN project "InDark". AGV is funded by "la Caixa" Foundation (ID 100010434) and the European Union's Horizon 2020 research and innovation programme under the Marie Sklodowska-Curie grant agreement No 847648, with fellowship code LCF/BQ/PI21/11830027. MM is also supported by the ASI/LiteBIRD grant n. 2020-9-HH.0 and by the Italian Research Center on High Performance Computing Big Data and Quantum Computing (ICSC), project funded by European Union - NextGenerationEU - and National Recovery and Resilience Plan (NRRP) - Mission 4 Component 2 within the activities of Spoke 3 (Astrophysics and Cosmos Observations). AF, MGD and AGV also acknowledge the participation in the COST Action CA21136 "Addressing observational tensions in cosmology with systematics and fundamental physics" (CosmoVerse).

Appendix A. Data sets

In this appendix, we present the tables with the GRBs and the CCH data employed in this work and described in Secs. 3.1 and 3.2, respectively.

Table A.1
Sub-sample of the 20 GRBs from the Platinum data set (Dainotti et al., 2020a) used in the calibration of the 3D and 2D Dainotti relations. T_X^* has units of s, while the fluxes $F_{\rm peak}$ and $F_{\rm X}$ are given in erg cm^{-2} s^{-1}. The K-corrections are dimensionless. For all the quantities we also report the associated 1σ error. All these objects are provided by the *third Swift GRB Catalog* (Lien et al., 2016), except for the 091018 and 131105A GRBs, which are from the *Swift BAT burst analyser* (Evans et al., 2010). We refer the reader to Table A1 of Cao et al. (2022a) for the remaining GRBs of the Platinum sample.

ID	z	$\log T_X^*$	$\sigma_{\log T_X^*}$	$F_{\rm peak}$	$\sigma_{F_{\rm peak}}$	$K_{\rm prompt}$	$\sigma_{K_{\rm prompt}}$	$\log F_X$	$\sigma_{\log F_X}$	$K_{\rm plateau}$	$\sigma_{K_{\rm plateau}}$
070521	0.553	3.361	0.048	8.71e-08	1.20e-08	0.662	0.053	-10.012	0.049	0.991	0.175
080430	0.767	3.970	0.038	1.82e-07	8.08e-09	0.868	0.036	-11.172	0.028	3.459	2.059
151027A	0.810	3.741	0.017	5.82e-07	2.88e-08	0.637	0.031	-9.935	0.022	0.956	0.021
070508	0.820	2.765	0.012	2.24e-06	3.07e-08	0.570	0.032	-9.161	0.011	0.868	0.012
060814	0.840	3.959	0.035	6.06e-07	1.48e-08	0.653	0.016	-10.911	0.035	0.982	0.036
140506A	0.889	3.031	0.069	8.67e-07	4.56e-08	0.664	0.105	-9.904	0.055	0.938	0.136
091018	0.971	2.602	0.034	5.91e-07	1.22e-08	1.140	0.030	-9.627	0.024	0.941	0.041
131030A	1.290	2.486	0.028	2.65e-06	4.61e-08	0.416	0.041	-9.294	0.025	0.775	0.017
061121	1.314	3.423	0.017	1.96e-06	2.43e-08	0.451	0.008	-10.030	0.013	0.958	0.037
150910A	1.360	3.481	0.029	8.28e-08	2.18e-08	0.632	0.309	-9.971	0.704	0.750	0.037
110213A	1.460	3.450	0.024	7.15e-08	1.88e-08	2.100	0.903	-9.897	0.036	1.187	0.295
060418	1.490	2.723	0.057	4.99e-07	1.63e-08	0.633	0.031	-9.793	0.049	0.982	0.122
070306	1.496	4.472	0.028	2.01e-07	8.99e-09	0.639	0.408	-11.274	0.034	0.857	0.040
090418A	1.608	3.112	0.031	1.58e-07	1.66e-08	0.508	0.082	-10.047	0.029	0.981	0.083
131105A	1.686	3.520	0.048	2.68e-07	2.04e-09	0.582	0.064	-10.911	0.033	0.942	0.093
091020	1.710	2.520	0.045	3.64e-07	1.71e-08	0.443	0.033	-9.713	0.034	0.901	0.067
150314A	1.758	2.052	0.016	3.81e-06	6.06e-08	0.297	0.033	-8.610	0.015	0.760	0.015
190106A	1.860	3.735	0.031	3.36e-07	1.30e-08	0.614	0.073	-10.432	0.029	2.675	2.089
060708	1.920	3.040	0.063	6.89e-08	7.96e-09	0.467	0.563	-10.869	0.061	1.682	0.803
160121A	1.960	3.353	0.120	7.79e-08	8.23e-09	0.822	0.136	-11.173	0.069	1.022	0.161

Table A.2
In this table, we present the 33 CCH data points used in this work, with the corresponding references. All the uncertainties are evaluated at 68% C.L. and, in the case of Refs. Moresco et al. (2012, 2016), the central values of $H(z)$ are computed by performing the arithmetic mean of the measurements obtained with the BC03 (Bruzual and Charlot, 2003) and MaStro (Maraston and Stromback, 2011) SPS models. We remind the reader that we incorporate in the analysis also the correlations through the covariance matrix from Moresco et al. (2020).

z	$H(z)$ [Km/s/Mpc]	References	z	$H(z)$ [Km/s/Mpc]	References
0.07	69.0 ± 19.6	(Zhang et al., 2014)	0.48	97.0 ± 62.0	(Stern et al., 2010)
0.09	69.0 ± 12.0	(Jiménez et al., 2003)	0.5929	107.0 ± 15.5	(Moresco et al., 2012)
0.12	68.6 ± 26.2	(Zhang et al., 2014)	0.6797	95.0 ± 10.5	(Moresco et al., 2012)
0.17	83.0 ± 8.0	(Simon et al., 2005)	0.75	98.8 ± 33.6	(Borghi et al., 2022)
0.1791	78.0 ± 6.2	(Moresco et al., 2012)	0.7812	96.5 ± 12.5	(Moresco et al., 2012)
0.1993	78.0 ± 6.9	(Moresco et al., 2012)	0.8754	124.5 ± 17.4	(Moresco et al., 2012)
0.2	72.9 ± 29.6	(Zhang et al., 2014)	0.88	90.0 ± 40.0	(Stern et al., 2010)
0.27	77.0 ± 14.0	(Simon et al., 2005)	0.9	117.0 ± 23.0	(Simon et al., 2005)
0.28	88.8 ± 36.6	(Zhang et al., 2014)	1.037	133.5 ± 17.6	(Moresco et al., 2012)
0.3519	85.5 ± 15.7	(Moresco et al., 2012)	1.26	135.0 ± 65.0	(Tomasetti et al., 2023)
0.3802	86.2 ± 14.6	(Moresco et al., 2016)	1.3	168.0 ± 17.0	(Simon et al., 2005)
0.4	95.0 ± 17.0	(Simon et al., 2005)	1.363	160.0 ± 33.8	(Moresco, 2015)
0.4004	79.9 ± 11.4	(Moresco et al., 2016)	1.43	177.0 ± 18.0	(Simon et al., 2005)
0.4247	90.4 ± 12.8	(Moresco et al., 2016)	1.53	140.0 ± 14.0	(Simon et al., 2005)
0.4497	96.3 ± 14.4	(Moresco et al., 2016)	1.75	202.0 ± 40.0	(Simon et al., 2005)
0.47	89.0 ± 49.6	(Ratsimbazafy et al., 2017)	1.965	186.5 ± 50.6	(Moresco, 2015)
0.4783	83.8 ± 10.2	(Moresco et al., 2016)			

Table B.1
p-values obtained from the KS and the AD tests performed to test if the sub-sample of 20 GRBs at $z \lesssim 2$ used to calibrate the Dainotti relations with CCH and the 50 GRBs from the full Platinum sample are likely to be obtained from the same parent distribution. This is our null hypothesis. All the *p*-values displayed in the table allow us not to reject the null hypothesis, since $p \geq 0.05$.

	$\log T_X^\star$	$F_{\rm peak}$	$K_{\rm prompt}$	$\log F_X$	$K_{\rm plateau}$
p-value (KS)	0.949	0.504	0.254	0.391	0.074
p-value (AD)	0.250	0.250	0.116	0.250	0.052

Appendix B. Kolmogorov-Smirnov and Anderson-Darling tests for the Platinum sample

In this appendix, we show the results of the KS and AD tests performed to ensure that the sub-sample of 20 GRBs used to calibrate the Dainotti relations with CCH at $z \lesssim 2$ are fairly representative of the entire population of GRBs (see Sec. 3.1). This is our null hypothesis. We apply the KS and AD tests to each variable of the Platinum sample employed in this work: $\log T_X^\star$, $F_{\rm peak}$, $K_{\rm prompt}$, $\log F_X$ and $K_{\rm plateau}$. We decide to not reject the null hypothesis if the *p*-value $p \geq 0.05$ and reject it if $p < 0.05$. The results of both the KS and the AD test are displayed in Table B.1. The *p*-values listed in the table show that we cannot reject the null hypothesis in all cases, regardless of the variable in the Platinum sample employed in the test.

Data availability

The data employed in this article are reported in the corresponding tables (see Appendix A and references therein).

References

Abdalla, E., et al., 2022. Cosmology intertwined: a review of the particle physics, astrophysics, and cosmology associated with the cosmological tensions and anomalies. J. High Energy Astrophys. 34, 49–211. https://doi.org/10.1016/j.jheap.2022.04.002. arXiv:2203.06142.

Aghanim, N., et al., Planck, 2020. Planck 2018 results. VI. Cosmological parameters. Astron. Astrophys. 641, A6. https://doi.org/10.1051/0004-6361/201833910. arXiv:1807.06209.

Alfano, A.C., Capozziello, S., Luongo, O., Muccino, M., 2024. Cosmological transition epoch from gamma-ray burst correlations. J. High Energy Astrophys. 42, 178–196. https://doi.org/10.1016/j.jheap.2024.05.002. arXiv:2402.18967.

Amati, L., et al., 2002. Intrinsic spectra and energetics of BeppoSAX gamma-ray bursts with known redshifts. Astron. Astrophys. 390, 81. https://doi.org/10.1051/0004-6361:20020722. arXiv:astro-ph/0205230.

Amati, L., Guidorzi, C., Frontera, F., Della Valle, M., Finelli, F., Landi, R., Montanari, E., 2008. Measuring the cosmological parameters with the $E_{p,i}$-E_{iso} correlation of gamma-ray bursts. Mon. Not. R. Astron. Soc. 391, 577–584. https://doi.org/10.1111/j.1365-2966.2008.13943.x. arXiv:0805.0377.

Amati, L., D'Agostino, R., Luongo, O., Muccino, M., Tantalo, M., 2019. Addressing the circularity problem in the $E_{\rm p} - E_{\rm iso}$ correlation of gamma-ray bursts. Mon. Not. R. Astron. Soc. 486, L46–L51. https://doi.org/10.1093/mnrasl/slz056. arXiv:1811.08934.

Amati, L., et al., THESEUS, 2021. The THESEUS space mission: science goals, requirements and mission concept. Exp. Astron. 52, 183–218. https://doi.org/10.1007/s10686-021-09807-8. arXiv:2104.09531.

Anderson, T.W., Darling, D.A., 1952. Asymptotic theory of certain "goodness-of-fit" criteria based on stochastic processes. Ann. Math. Stat. 23, 193–212.

Atteia, J.L., Cordier, B., Wei, J.S.VO. M, 2022. The SVOM mission. Int. J. Mod. Phys. D 31, 2230008. https://doi.org/10.1142/S0218271822300087. arXiv:2203.10962.

Banados, E., et al., 2018. An 800-million-solar-mass black hole in a significantly neutral Universe at redshift 7.5. Nature 553, 473–476. https://doi.org/10.1038/nature25180. arXiv:1712.01860.

Bargiacchi, G., Risaliti, G., Benetti, M., Capozziello, S., Lusso, E., Saccardi, A., Signorini, M., 2021. Cosmography by orthogonalized logarithmic polynomials. Astron. Astrophys. 649, A65. https://doi.org/10.1051/0004-6361/202140386. arXiv:2101.08278.

Bargiacchi, G., Dainotti, M., Nagataki, S., Capozziello, S., 2023. Gamma-ray bursts, quasars, baryonic acoustic oscillations, and supernovae Ia: new statistical insights and cosmological constraints. Mon. Not. R. Astron. Soc. 521, 3909–3924.

Bernardini, M.G., 2015. Gamma-ray bursts and magnetars: observational signatures and predictions. J. High Energy Astrophys. 7, 64–72.

Borghi, N., Moresco, M., Cimatti, A., 2022. Toward a better understanding of cosmic chronometers: a new measurement of H(z) at z ∼ 0.7. Astrophys. J. Lett. 928, L4. https://doi.org/10.3847/2041-8213/ac3fb2. arXiv:2110.04304.

Bruzual, G., Charlot, S., 2003. Stellar population synthesis at the resolution of 2003. Mon. Not. R. Astron. Soc. 344, 1000. https://doi.org/10.1046/j.1365-8711.2003.06897.x. arXiv:astro-ph/0309134.

Cannizzo, J., Troja, E., Gehrels, N., 2011. Fall-back disks in long and short GRBs. arXiv preprint. arXiv:1104.0456.

Cannizzo, J.K., Gehrels, N., 2009. A new paradigm for gamma-ray bursts: long-term accretion rate modulation by an external accretion disk. Astrophys. J. 700, 1047.

Cao, S., Dainotti, M., Ratra, B., 2022a. Gamma-ray burst data strongly favor the three-parameter fundamental plane (Dainotti) correlation relation over the two-parameter one. Mon. Not. R. Astron. Soc. 516, 1386–1405. https://doi.org/10.1093/mnras/stac2170. http://arxiv.org/abs/2204.08710.

Cao, S., Dainotti, M., Ratra, B., 2022b. Standardizing Platinum Dainotti-correlated gamma-ray bursts, and using them with standardized Amati-correlated gamma-ray bursts to constrain cosmological model parameters. Mon. Not. R. Astron. Soc. 512, 439–454. https://doi.org/10.1093/mnras/stac517. arXiv:2201.05245.

Cardone, V.F., Capozziello, S., Dainotti, M.G., 2009. An updated gamma ray bursts Hubble diagram. Mon. Not. R. Astron. Soc. 400, 775–790. https://doi.org/10.1111/j.1365-2966.2009.15456.x. arXiv:0901.3194.

Cardone, V.F., Dainotti, M.G., Capozziello, S., Willingale, R., 2010. Constraining cosmological parameters by gamma-ray burst X-ray afterglow light curves. Mon. Not. R. Astron. Soc. 408, 1181–1186. https://doi.org/10.1111/j.1365-2966.2010.17197.x. arXiv:1005.0122.

Colgáin, E.O., Sheikh-Jabbari, M.M., Solomon, R., Bargiacchi, G., Capozziello, S., Dainotti, M.G., Stojkovic, D., 2022. Revealing intrinsic flat ΛCDM biases with standardizable candles. Phys. Rev. D 106, L041301. https://doi.org/10.1103/PhysRevD.106.L041301. arXiv:2203.10558.

Collazzi, A.C., Schaefer, B.E., Goldstein, A., Preece, R.D., 2012. A significant problem with using the Amati relation for cosmological purposes. Astrophys. J. 747, 39. https://doi.org/10.1088/0004-637X/747/1/39. arXiv:1112.4347.

Collett, T., Montanari, F., Rasanen, S., 2019. Model-independent determination of H_0 and Ω_{K0} from strong lensing and type Ia supernovae. Phys. Rev. Lett. 123, 231101. https://doi.org/10.1103/PhysRevLett.123.231101. arXiv:1905.09781.

Cucchiara, A., et al., 2011. Constraining GRB emission physics with extensive early-time, multiband follow-up. Astrophys. J. 743, 154. https://doi.org/10.1088/0004-637X/743/2/154. arXiv:1107.3352.

D'Agostini, G., 2005. Fits, and especially linear fits, with errors on both axes, extra variance of the data points and other complications. https://doi.org/10.48550/arXiv.physics/0511182. arXiv:physics/0511182, 2005.

Dai, Z.G., Lu, T., 1998. Gamma-ray burst afterglows and evolution of postburst fireballs with energy injection from strongly magnetic millisecond pulsars. Astron. Astrophys. 333, L87. arXiv:astro-ph/9810402.

Dainotti, M., Del Vecchio, R., 2017. Gamma ray burst afterglow and prompt-afterglow relations: an overview. New Astron. Rev. 77, 23–61. https://doi.org/10.1016/j.newar.2017.04.001. arXiv:1703.06876.

Dainotti, M.G., Amati, L., 2018. Gamma-ray burst prompt correlations: selection and instrumental effects. Publ. Astron. Soc. Pac. 130, 051001. https://doi.org/10.1088/1538-3873/aaa8d7. arXiv:1704.00844.

Dainotti, M.G., Cardone, V.F., Capozziello, S., 2008. A time - luminosity correlation for gamma ray bursts in the X - rays. Mon. Not. R. Astron. Soc. 391, 79. https://doi.org/10.1111/j.1745-3933.2008.00560.x. arXiv:0809.1389.

Dainotti, M.G., Willingale, R., Capozziello, S., Cardone, V.F., Ostrowski, M., 2010. Discovery of a tight correlation for gamma ray burst afterglows with 'canonical' light curves. Astrophys. J. Lett. 722, L215. https://doi.org/10.1088/2041-8205/722/2/L215. arXiv:1009.1663.

Dainotti, M.G., Cardone, V.F., Capozziello, S., Ostrowski, M., Willingale, R., 2011a. Study of possible systematics in the L*X - Ta* correlation of gamma ray bursts. Astrophys. J. 730, 135. https://doi.org/10.1088/0004-637X/730/2/135. arXiv:1101.1676.

Dainotti, M.G., Ostrowski, M., Willingale, R., 2011b. Towards a standard gamma-ray burst: tight correlations between the prompt and the afterglow plateau phase emission. Mon. Not. R. Astron. Soc. 418, 2202–2206.

Dainotti, M.G., Cardone, V.F., Piedipalumbo, E., Capozziello, S., 2013a. Slope evolution of GRB correlations and cosmology. Mon. Not. R. Astron. Soc. 436, 82–88. https://doi.org/10.1093/mnras/stt1516.

Dainotti, M.G., Petrosian, V., Singal, J., Ostrowski, M., 2013b. Determination of the intrinsic luminosity time correlation in the X-ray afterglows of gamma-ray bursts. Astrophys. J. 774, 157. https://doi.org/10.1088/0004-637X/774/2/157. arXiv:1307.7297.

Dainotti, M.G., Del Vecchio, R., Shigehiro, N., Capozziello, S., 2015a. Selection effects in gamma-ray burst correlations: consequences on the ratio between gamma-ray burst and star formation rates. Astrophys. J. 800, 31. https://doi.org/10.1088/0004-637X/800/1/31. arXiv:1412.3969.

Dainotti, M.G., Petrosian, V., Willingale, R., O'Brien, P., Ostrowski, M., Nagataki, S., 2015b. Luminosity–time and luminosity–luminosity correlations for GRB prompt and afterglow plateau emissions. Mon. Not. R. Astron. Soc. 451, 3898–3908. https://doi.org/10.1093/mnras/stv1229. arXiv:1506.00702.

Dainotti, M.G., Postnikov, S., Hernandez, X., Ostrowski, M., 2016. A fundamental plane for gamma-ray bursts with X-ray plateaus. Astrophys. J. 825, L20. https://doi.org/10.3847/2041-8205/825/2/l20.

Dainotti, M.G., Hernandez, X., Postnikov, S., Nagataki, S., O'brien, P., Willingale, R., Striegel, S., 2017a. A study of the gamma-ray burst fundamental plane. Astrophys. J. 848, 88. https://doi.org/10.3847/1538-4357/aa8a6b.

Dainotti, M.G., Nagataki, S., Maeda, K., Postnikov, S., Pian, E., 2017b. A study of gamma ray bursts with afterglow plateau phases associated with supernovae. Astron. Astrophys. 600, A98. https://doi.org/10.1051/0004-6361/201628384. arXiv:1612.02917.

Dainotti, M.G., Del Vecchio, R., Tarnopolski, M., 2018. Gamma-ray burst prompt correlations. Adv. Astron. 2018, 4969503. https://doi.org/10.1155/2018/4969503.

Dainotti, M.G., Lenart, A., Sarracino, G., Nagataki, S., Capozziello, S., Fraija, N., 2020a. The X-ray fundamental plane of the platinum sample, the kilonovae and the SNe Ib/c associated with GRBs. Astrophys. J. 904, 97. https://doi.org/10.3847/1538-4357/abbe8a. arXiv:2010.02092.

Dainotti, M.G., Livermore, S., Kann, D.A., Li, L., Oates, S., Yi, S., Zhang, B., Gendre, B., Cenko, B., Fraija, N., 2020b. The optical luminosity–time correlation for more than 100 gamma-ray burst afterglows. Astrophys. J. Lett. 905, L26. https://doi.org/10.3847/2041-8213/abcda9. arXiv:2011.14493.

Dainotti, M.G., Simone, B.D., Schiavone, T., Montani, G., Rinaldi, E., Lambiase, G., 2021. On the Hubble constant tension in the SNe Ia Pantheon sample. Astrophys. J. 912, 150. https://doi.org/10.3847/1538-4357/abeb73.

Dainotti, M.G., Lenart, A.L., Chraya, A., Sarracino, G., Nagataki, S., Fraija, N., Capozziello, S., Bogdan, M., 2022a. The gamma-ray bursts fundamental plane correlation as a cosmological tool. Mon. Not. R. Astron. Soc. https://doi.org/10.1093/mnras/stac2752. arXiv:2209.08675.

Dainotti, M.G., Nielson, V., Sarracino, G., Rinaldi, E., Nagataki, S., Capozziello, S., Gnedin, O.Y., Bargiacchi, G., 2022b. Optical and X-ray GRB fundamental planes as cosmological distance indicators. Mon. Not. R. Astron. Soc. 514, 1828–1856. https://doi.org/10.1093/mnras/stac1141.

Dainotti, M.G., Sarracino, G., Capozziello, S., 2022c. Gamma-ray bursts, supernovae Ia, and baryon acoustic oscillations: a binned cosmological analysis. Publ. Astron. Soc. Jpn. 74, 1095–1113–1113. https://doi.org/10.1093/pasj/psac057. arXiv:2206.07479.

Dainotti, M.G., et al., 2022d. The optical two- and three-dimensional fundamental plane correlations for nearly 180 gamma-ray burst afterglows with Swift/UVOT, RATIR, and the Subaru telescope. Astrophys. J. Suppl. 261, 25. https://doi.org/10.3847/1538-4365/ac7c64. arXiv:2203.12908.

Dainotti, M.G., De Simone, B., Schiavone, T., Montani, G., Rinaldi, E., Lambiase, G., Bogdan, M., Ugale, S., 2022e. On the evolution of the Hubble constant with the SNe Ia Pantheon sample and baryon acoustic oscillations: a feasibility study for GRB-cosmology in 2030. Galaxies 10, 24–66. https://doi.org/10.3390/galaxies10010024. arXiv:2201.09848.

Dainotti, M.G., Bargiacchi, G., Lenart, A.L., Capozziello, S., Colgain, E.O., Solomon, R., Stojkovic, D., Sheikh-Jabbari, M.M., 2022f. Quasar standardization: overcoming selection biases and redshift evolution. Astrophys. J. 931, 106. https://doi.org/10.3847/1538-4357/ac6593. arXiv:2203.12914.

Dainotti, M.G., Bargiacchi, G., Bogdan, M., Lenart, A.L., Iwasaki, K., Capozziello, S., Zhang, B., Fraija, N., 2023. Reducing the uncertainty on the Hubble constant up to 35% with an improved statistical analysis: different best-fit likelihoods for type Ia supernovae, baryon acoustic oscillations, quasars, and gamma-ray bursts. Astrophys. J. 951, 63. https://doi.org/10.3847/1538-4357/acd63f. arXiv:2305.10030.

Dainotti, M.G., Bargiacchi, G., Bogdan, M., Capozziello, S., Nagataki, S., 2024. On the statistical assumption on the distance moduli of supernovae Ia and its impact on the determination of cosmological parameters. J. High Energy Astrophys. 41, 30–41. https://doi.org/10.1016/j.jheap.2024.01.001.

Dall'Osso, S., Stratta, G., Guetta, D., Covino, S., De Cesare, G., Stella, L., 2010. GRB afterglows with energy injection from a spinning down NS. arXiv preprint. arXiv:1004.2788.

Dall'Osso, S., Stratta, G., Perna, R., de Cesare, G., Stella, L., 2023. Magnetar central engines in gamma-ray bursts follow the universal relation of accreting magnetic stars. Astrophys. J. Lett. 949, L32. https://doi.org/10.3847/2041-8213/acccec. arXiv:2305.00029.

de Cruz Pérez, J., Park, C.G., Ratra, B., 2023. Current data are consistent with flat spatial hypersurfaces in the ΛCDM cosmological model but favor more lensing than the model predicts. Phys. Rev. D 107, 063522. https://doi.org/10.1103/PhysRevD.107.063522. arXiv:2211.04268.

de Cruz Pérez, J., Park, C.G., Ratra, B., 2024. Updated observational constraints on spatially flat and nonflat ΛCDM and XCDM cosmological models. Phys. Rev. D 110, 023506. https://doi.org/10.1103/PhysRevD.110.023506. arXiv:2404.19194.

Dhawan, S., Alsing, J., Vagnozzi, S., 2021. Non-parametric spatial curvature inference using late-Universe cosmological probes. Mon. Not. R. Astron. Soc. 506, L1–L5. https://doi.org/10.1093/mnrasl/slab058. arXiv:2104.02485.

Di Valentino, E., Melchiorri, A., Silk, J., 2019. Planck evidence for a closed Universe and a possible crisis for cosmology. Nat. Astron. 4, 196–203. https://doi.org/10.1038/s41550-019-0906-9. arXiv:1911.02087.

Di Valentino, E., Mena, O., Pan, S., Visinelli, L., Yang, W., Melchiorri, A., Mota, D.F., Riess, A.G., Silk, J., 2021a. In the realm of the Hubble tension-a review of solutions. Class. Quantum Gravity 38, 153001. https://doi.org/10.1088/1361-6382/ac086d. arXiv:2103.01183.

Di Valentino, E., et al., 2021b. Snowmass2021 - letter of interest cosmology intertwined IV: the age of the universe and its curvature. Astropart. Phys. 131, 102607. https://doi.org/10.1016/j.astropartphys.2021.102607. arXiv:2008.11286.

Dinda, B.R., 2023. Minimal model-dependent constraints on cosmological nuisance parameters and cosmic curvature from combinations of cosmological data. Int. J. Mod. Phys. D 32, 2350079. https://doi.org/10.1142/S0218271823500797. arXiv:2209.14639.

Efron, B., Petrosian, V., 1992. A simple test of independence for truncated data with applications to redshift surveys. Astrophys. J. 399, 345. https://doi.org/10.1086/171931.

Efstathiou, G., Gratton, S., 2020. The evidence for a spatially flat Universe. Mon. Not. R. Astron. Soc. 496, L91–L95. https://doi.org/10.1093/mnrasl/slaa093. arXiv:2002.06892.

Evans, P.A., et al., 2010. The Swift burst analyser I: BAT and XRT spectral and flux evolution of gamma ray bursts. Astron. Astrophys. 519, A102. https://doi.org/10.1051/0004-6361/201014819. arXiv:1004.3208.

Favale, A., Gómez-Valent, A., Migliaccio, M., 2023. Cosmic chronometers to calibrate the ladders and measure the curvature of the Universe. A model-independent study. Mon. Not. R. Astron. Soc. 523, 3406–3422. https://doi.org/10.1093/mnras/stad1621. arXiv:2301.09591.

Foreman-Mackey, D., Hogg, D.W., Lang, D., Goodman, J., 2013. emcee: the MCMC hammer. Publ. Astron. Soc. Pac. 125, 306–312. https://doi.org/10.1086/670067.

Freedman, W.L., 2021. Measurements of the Hubble constant: tensions in perspective. Astrophys. J. 919, 16. https://doi.org/10.3847/1538-4357/ac0e95.

Freedman, W.L., Madore, B.F., 2023. Progress in direct measurements of the Hubble constant. J. Cosmol. Astropart. Phys. 11, 050. https://doi.org/10.1088/1475-7516/2023/11/050. arXiv:2309.05618.

Freedman, W.L., Madore, B.F., Hoyt, T., Jang, I.S., Beaton, R., Lee, M.G., Monson, A., Neeley, J., Rich, J., 2020. Calibration of the tip of the red giant branch. Astrophys. J. 891, 57.

Ghirlanda, G., Ghisellini, G., Lazzati, D., Firmani, C., 2004. Gamma-ray bursts: new rulers to measure the universe. Astrophys. J. 613, L13.

Ghirlanda, G., Ghisellini, G., Firmani, C., 2006. Gamma-ray bursts as standard candles to constrain the cosmological parameters. New J. Phys. 8, 123.

Ghirlanda, G., Nava, L., Ghisellini, G., Celotti, A., Burlon, D., Covino, S., Melandri, A., 2012. Gamma ray bursts in the comoving frame. Mon. Not. R. Astron. Soc. 420, 483. https://doi.org/10.1111/j.1365-2966.2011.20053.x. arXiv:1107.4096.

Ghisellini, G., Ghirlanda, G., Firmani, C., Lazzati, D., Avila-Reese, V., 2005. Cosmology with gamma-ray bursts. Nuovo Cimento C 28, 639–646. https://doi.org/10.1393/ncc/i2005-10119-0.

Gómez-Valent, A., 2022. Measuring the sound horizon and absolute magnitude of SNIa by maximizing the consistency between low-redshift data sets. Phys. Rev. D 105, 043528. https://doi.org/10.1103/PhysRevD.105.043528. arXiv:2111.15450.

Gómez-Valent, A., Amendola, L., 2018. H_0 from cosmic chronometers and type Ia supernovae, with Gaussian processes and the novel weighted polynomial regression method. J. Cosmol. Astropart. Phys. 04, 051. https://doi.org/10.1088/1475-7516/2018/04/051. arXiv:1802.01505.

Gómez-Valent, A., Favale, A., Migliaccio, M., Sen, A.A., 2024. Late-time phenomenology required to solve the H0 tension in view of the cosmic ladders and the anisotropic and angular BAO datasets. Phys. Rev. D 109, 023525. https://doi.org/10.1103/PhysRevD.109.023525. arXiv:2309.07795.

Goodman, J., Weare, J., 2010. Ensemble samplers with affine invariance. Commun. Appl. Math. Comput. Sci. 5, 65–80. https://doi.org/10.2140/camcos.2010.5.65.

Govindaraj, G., Desai, S., 2022. Low redshift calibration of the Amati relation using galaxy clusters. J. Cosmol. Astropart. Phys. 2022, 069.

Handley, W., 2021. Curvature tension: evidence for a closed universe. Phys. Rev. D 103, L041301. https://doi.org/10.1103/PhysRevD.103.L041301. arXiv:1908.09139.

Haridasu, B.S., Luković, V.V., Moresco, M., Vittorio, N., 2018. An improved model-independent assessment of the late-time cosmic expansion. J. Cosmol. Astropart. Phys. 10, 015. https://doi.org/10.1088/1475-7516/2018/10/015. arXiv:1805.03595.

Hascoet, R., Daigne, F., Mochkovitch, R., 2014. The prompt–early afterglow connection in gamma-ray bursts: implications for the early afterglow physics. Mon. Not. R. Astron. Soc. 442, 20–27. https://doi.org/10.1093/mnras/stu750. arXiv:1401.0751.

Heavens, A., Jiménez, R., Verde, L., 2014. Standard rulers, candles, and clocks from the low-redshift Universe. Phys. Rev. Lett. 113, 241302. https://doi.org/10.1103/PhysRevLett.113.241302. arXiv:1409.6217.

Heussaff, V., Atteia, J.L., Zolnierowski, Y., 2013. The Epeak-Eiso relation revisited with Fermi GRBs: resolving a long-standing debate? Astron. Astrophys. 557, A100. https://doi.org/10.1051/0004-6361/201321528. arXiv:1306.1757.

Hu, J.P., Wang, F.Y., Dai, Z.G., 2021. Measuring cosmological parameters with a luminosity–time correlation of gamma-ray bursts. Mon. Not. R. Astron. Soc. 507, 730–742. https://doi.org/10.1093/mnras/stab2180.

Hwang, S.g., L'Huillier, B., Keeley, R.E., Jee, M.J., Shafieloo, A., 2023. How to use GP: effects of the mean function and hyperparameter selection on Gaussian process regression. J. Cosmol. Astropart. Phys. 02, 014. https://doi.org/10.1088/1475-7516/2023/02/014. arXiv:2206.15081.

Jiménez, R., Loeb, A., 2002. Constraining cosmological parameters based on relative galaxy ages. Astrophys. J. 573, 37–42. https://doi.org/10.1086/340549. arXiv:astro-ph/0106145.

Jiménez, R., Verde, L., Treu, T., Stern, D., 2003. Constraints on the equation of state of dark energy and the Hubble constant from stellar ages and the CMB. Astrophys. J. 593, 622–629. https://doi.org/10.1086/376595. arXiv:astro-ph/0302560.

Kelly, B.C., 2007. Some aspects of measurement error in linear regression of astronomical data. Astrophys. J. 665, 1489–1506. https://doi.org/10.1086/519947. arXiv:0705.2774.

Khadka, N., Ratra, B., 2020. Constraints on cosmological parameters from gamma-ray burst peak photon energy and bolometric fluence measurements and other data. Mon. Not. R. Astron. Soc. 499, 391–403. https://doi.org/10.1093/mnras/staa2779.

Khadka, N., Luongo, O., Muccino, M., Ratra, B., 2021. Do gamma-ray burst measurements provide a useful test of cosmological models? J. Cosmol. Astropart. Phys. 09, 042. https://doi.org/10.1088/1475-7516/2021/09/042. arXiv:2105.12692.

Kolmogorov, A., 1933. Sulla determinazione empirica di una legge di distribuzione. G. Ist. Ital. Attuari 4, 89–91.

Kumar, D., Rani, N., Jain, D., Mahajan, S., Mukherjee, A., 2023. Gamma rays bursts: a viable cosmological probe? J. Cosmol. Astropart. Phys. 2023, 021. https://doi.org/10.1088/1475-7516/2023/07/021. arXiv:2212.05731 [astro-ph].

Labbe, I., et al., 2023. A population of red candidate massive galaxies ~600 Myr after the Big Bang. Nature 616, 266–269. https://doi.org/10.1038/s41586-023-05786-2. arXiv:2207.12446.

Lamb, D.Q., 2003. Gamma-ray bursts as a probe of cosmology. AIP Conf. Proc. 662, 433–437. https://doi.org/10.1063/1.1579395. arXiv:astro-ph/0210434.

Lenart, A.L., Bargiacchi, G., Dainotti, M.G., Nagataki, S., Capozziello, S., 2023. A bias-free cosmological analysis with quasars alleviating H_0 tension. Astrophys. J. Suppl. 264, 46. https://doi.org/10.3847/1538-4365/aca404. arXiv:2211.10785.

Lewis, A., 2019. GetDist: a Python package for analysing Monte Carlo samples. arXiv:1910.13970.

Li, H., Xia, J.Q., Liu, J., Zhao, G.B., Fan, Z.H., Zhang, X., 2008. Overcoming the circular problem for gamma-ray bursts in cosmological global-fitting analysis. Astrophys. J. 680, 92.

Li, Z., Zhang, B., Liang, N., 2023. Testing dark energy models with gamma-ray bursts calibrated from the observational $h(z)$ data through a Gaussian process. Mon. Not. R. Astron. Soc. 521, 4406–4413. https://doi.org/10.1093/mnras/stad838. arXiv:2212.14291 [astro-ph].

Liang, E.W., Yi, S.x., Zhang, J., LV, H.J., Zhang, B.B., Zhang, B., 2010. Constraining GRB initial Lorentz factor with the afterglow onset feature and discovery of a tight gamma_0-e_iso correlation. Astrophys. J. 725, 2209–2224. https://doi.org/10.1088/0004-637X/725/2/2209. arXiv:0912.4800.

Liang, N., Xiao, W.K., Liu, Y., Zhang, S.N., 2008. A cosmology-independent calibration of gamma-ray burst luminosity relations and the Hubble diagram. Astrophys. J. 685, 354.

Liang, N., Li, Z., Xie, X., Wu, P., 2022. Calibrating gamma-ray bursts by using a Gaussian process with type Ia supernovae. Astrophys. J. 941, 84. https://doi.org/10.3847/1538-4357/aca08a.

Lien, A., et al., 2016. The third Swift burst alert telescope gamma-ray burst catalog. Astrophys. J. 829, 7. https://doi.org/10.3847/0004-637X/829/1/7. arXiv:1606.01956.

Liu, Y., Liang, N., Xie, X., Yuan, Z., Yu, H., Wu, P., 2022. Gamma-ray burst constraints on cosmological models from the improved Amati correlation. Astrophys. J. 935, 7. https://doi.org/10.3847/1538-4357/ac7de5.

Luongo, O., Muccino, M., 2020. Kinematic constraints beyond $z \simeq 0$ using calibrated GRB correlations. Astron. Astrophys. 641, A174. https://doi.org/10.1051/0004-6361/202038264. arXiv:2010.05218.

Luongo, O., Muccino, M., 2021. Model-independent calibrations of gamma-ray bursts using machine learning. Mon. Not. R. Astron. Soc. 503, 4581–4600. https://doi.org/10.1093/mnras/stab795. arXiv:2011.13590.

Luongo, O., Muccino, M., 2022. Intermediate redshift calibration of gamma-ray bursts and cosmic constraints in non-flat cosmology. Mon. Not. R. Astron. Soc. 518, 2247–2255. https://doi.org/10.1093/mnras/stac2925.

Lusso, E., Piedipalumbo, E., Risaliti, G., Paolillo, M., Bisogni, S., Nardini, E., Amati, L., 2019. Tension with the flat ΛCDM model from a high-redshift Hubble diagram of supernovae, quasars, and gamma-ray bursts. Astron. Astrophys. 628, L4. https://doi.org/10.1051/0004-6361/201936223. arXiv:1907.07692.

Lusso, E., et al., 2020. Quasars as standard candles III. Validation of a new sample for cosmological studies. Astron. Astrophys. 642, A150. https://doi.org/10.1051/0004-6361/202038899. arXiv:2008.08586.

Malmquist, K.G., 1922. On Some Relations in Stellar Statistics. Meddelanden Fran Lunds Astronomiska Observatorium Serie I, vol. 100, pp. 1–52.

Maraston, C., Stromback, G., 2011. Stellar population models at high spectral resolution. Mon. Not. R. Astron. Soc. 418, 2785. https://doi.org/10.1111/j.1365-2966.2011.19738.x. arXiv:1109.0543.

Montiel, A., Cabrera, J.I., Hidalgo, J.C., 2020. Improving sampling and calibration of gamma-ray bursts as distance indicators. Mon. Not. R. Astron. Soc. 501, 3515–3526. https://doi.org/10.1093/mnras/staa3926.

Moresco, M., 2015. Raising the bar: new constraints on the Hubble parameter with cosmic chronometers at z ~ 2. Mon. Not. R. Astron. Soc. 450, L16–L20. https://doi.org/10.1093/mnrasl/slv037. arXiv:1503.01116.

Moresco, M., et al., 2012. Improved constraints on the expansion rate of the Universe up to z~1.1 from the spectroscopic evolution of cosmic chronometers. J. Cosmol. Astropart. Phys. 08, 006. https://doi.org/10.1088/1475-7516/2012/08/006. arXiv:1201.3609.

Moresco, M., Pozzetti, L., Cimatti, A., Jiménez, R., Maraston, C., Verde, L., Thomas, D., Citro, A., Tojeiro, R., Wilkinson, D., 2016. A 6% measurement of the Hubble parameter at $z \sim 0.45$: direct evidence of the epoch of cosmic re-acceleration. J. Cosmol. Astropart. Phys. 05, 014. https://doi.org/10.1088/1475-7516/2016/05/014. arXiv:1601.01701.

Moresco, M., Jiménez, R., Verde, L., Cimatti, A., Pozzetti, L., 2020. Setting the stage for cosmic chronometers. II. Impact of stellar population synthesis models systematics and full covariance matrix. Astrophys. J. 898, 82. https://doi.org/10.3847/1538-4357/ab9eb0. arXiv:2003.07362.

Moresco, M., et al., 2022. Unveiling the Universe with emerging cosmological probes. Living Rev. Relativ. 25, 6. https://doi.org/10.1007/s41114-022-00040-z. arXiv:2201.07241.

Mu, Y., Chang, B., Xu, L., 2023. Cosmography via Gaussian process with gamma ray bursts. J. Cosmol. Astropart. Phys. 09, 041. https://doi.org/10.1088/1475-7516/2023/09/041. arXiv:2302.02559.

Mukherjee, P., Dialektopoulos, K.F., Levi Said, J., Mifsud, J., 2024. A possible late-time transition of M_B inferred via neural networks. J. Cosmol. Astropart. Phys. 09, 060. https://doi.org/10.1088/1475-7516/2024/09/060. arXiv:2402.10502.

Norris, J.P., Marani, G.F., Bonnell, J.T., 2000. Connection between energy dependent lags and Lorentz factor in gamma-ray bursts. Astrophys. J. 534, 248–257. https://doi.org/10.1086/308725. arXiv:astro-ph/9903233.

Parsotan, T., Ito, H., 2022. GRB prompt emission: observed correlations and their interpretations. Universe 8, 310. https://doi.org/10.3390/universe8060310. arXiv:2204.09729.

Perivolaropoulos, L., Skara, F., 2022. Challenges for ΛCDM: an update. New Astron. Rev. 95, 101659. https://doi.org/10.1016/j.newar.2022.101659. arXiv:2105.05208.

Perlmutter, S., et al., Supernova Cosmology Project, 1999. Measurements of Ω and Λ from 42 high redshift supernovae. Astrophys. J. 517, 565–586. https://doi.org/10.1086/307221. arXiv:astro-ph/9812133.

Petrosian, V., Kitanidis, E., Kocevski, D., 2015. Cosmological evolution of long gamma-ray bursts and the star formation rate. Astrophys. J. 806, 44. https://doi.org/10.1088/0004-637X/806/1/44. arXiv:1504.01414.

Postnikov, S., Dainotti, M.G., Hernandez, X., Capozziello, S., 2014. Nonparametric study of the evolution of the cosmological equation of state with SNeIa, BAO, and high-redshift GRBs. Astrophys. J. 783, 126. https://doi.org/10.1088/0004-637X/783/2/126. arXiv:1401.2939.

Qi, J.Z., Meng, P., Zhang, J.F., Zhang, X., 2023. Model-independent measurement of cosmic curvature with the latest H(z) and SNe Ia data: a comprehensive investigation. Phys. Rev. D 108, 063522. https://doi.org/10.1103/PhysRevD.108.063522. arXiv:2302.08889.

Rasmussen, C.E., Williams, C.K.I., 2006. Gaussian Processes for Machine Learning. MIT Press.

Ratsimbazafy, A., Loubser, S., Crawford, S., Cress, C., Bassett, B., Nichol, R., Väisänen, P., 2017. Age-dating luminous red galaxies observed with the Southern African Large Telescope. Mon. Not. R. Astron. Soc. 467, 3239–3254. https://doi.org/10.1093/mnras/stx301. arXiv:1702.00418.

Rea, N., Gullon, M., Pons, J.A., Perna, R., Dainotti, M.G., Miralles, J.A., Torres, D.F., 2015. Constraining the GRB-magnetar model by means of the Galactic pulsar population. Astrophys. J. 813, 92. https://doi.org/10.1088/0004-637X/813/2/92. arXiv:1510.01430.

Riess, A., Anderson, R.I., Breuval, L., Casertano, S., Macri, L.M., Scolnic, D., Yuan, W., 2021. Uncrowding the Cepheids for an improved determination of the Hubble constant. JWST Proposal. Cycle 1 p. 1685.

Riess, A.G., Breuval, L., 2022. The local value of H0. In: IAU Symp., vol. 376, pp. 15–29. arXiv:2308.10954.

Riess, A.G., et al., Supernova Search Team, 1998. Observational evidence from supernovae for an accelerating universe and a cosmological constant. Astron. J. 116, 1009–1038. https://doi.org/10.1086/300499. arXiv:astro-ph/9805201.

Riess, A.G., et al., 2022. A comprehensive measurement of the local value of the Hubble constant with 1 km/s/Mpc uncertainty from the Hubble space telescope and the SH0ES team. Astrophys. J. Lett. 934, L7. https://doi.org/10.3847/2041-8213/ac5c5b. arXiv:2112.04510.

Risaliti, G., Lusso, E., 2015. A Hubble diagram for quasars. Astrophys. J. 815, 33. https://doi.org/10.1088/0004-637X/815/1/33. arXiv:1505.07118.

Risaliti, G., Lusso, E., 2017. Cosmology with AGN: can we use quasars as standard candles? Astron. Nachr. 338, 329–333. https://doi.org/10.1002/asna.201713351. arXiv:1612.02838.

Risaliti, G., Lusso, E., 2019. Cosmological constraints from the Hubble diagram of quasars at high redshifts. Nat. Astron. 3, 272–277. https://doi.org/10.1038/s41550-018-0657-z. arXiv:1811.02590.

Rowlinson, A., Gompertz, B.P., Dainotti, M., O'Brien, P.T., Wijers, R.A.M.J., van der Horst, A.J., 2014. Constraining properties of GRB magnetar central engines using the observed plateau luminosity and duration correlation. Mon. Not. R. Astron. Soc. 443, 1779–1787. https://doi.org/10.1093/mnras/stu1277. arXiv:1407.1053.

Sakamoto, T., et al., 2011. The second Swift BAT gamma-ray burst catalog. Astrophys. J. Suppl. 195, 2. https://doi.org/10.1088/0067-0049/195/1/2. arXiv:1104.4689.

Seikel, M., Clarkson, C., Smith, M., 2012. Reconstruction of dark energy and expansion dynamics using Gaussian processes. J. Cosmol. Astropart. Phys. 06, 036. https://doi.org/10.1088/1475-7516/2012/06/036. arXiv:1204.2832.

Signorini, M., Risaliti, G., Sacchi, A., Lusso, E., Nardini, E., 2023. Building the high-redshift Hubble diagram with quasars. In: Memorie della Societa Astronomica Italiana, p. 259. arXiv:2401.07909.

Simon, J., Verde, L., Jiménez, R., 2005. Constraints on the redshift dependence of the dark energy potential. Phys. Rev. D 71, 123001. https://doi.org/10.1103/PhysRevD.71.123001. arXiv:astro-ph/0412269.

Smirnov, N.V., 1939. Estimate of deviation between empirical distribution functions in two independent samples. Bull. Mosc. Univ. 2, 3–16.

Stern, D., Jiménez, R., Verde, L., Kamionkowski, M., Stanford, S., 2010. Cosmic chronometers: constraining the equation of state of dark energy. I: H(z) measurements. J. Cosmol. Astropart. Phys. 02, 008. https://doi.org/10.1088/1475-7516/2010/02/008. arXiv:0907.3149.

Stratta, G., Dainotti, M.G., Dall'Osso, S., Hernandez, X., De Cesare, G., 2018. On the magnetar origin of the GRBs presenting X-ray afterglow plateaus. Astrophys. J. 869, 155. https://doi.org/10.3847/1538-4357/aadd8f. arXiv:1804.08652.

Tian, X., Li, J.L., Yi, S.X., Yang, Y.P., Hu, J.P., Qu, Y.K., Wang, F.Y., 2023. Radio plateaus in gamma-ray burst afterglows and their application in cosmology. Astrophys. J. 958, 74. https://doi.org/10.3847/1538-4357/acfed8. arXiv:2310.00596.

Tomasetti, E., Moresco, M., Borghi, N., Jiao, K., Cimatti, A., Pozzetti, L., Carnall, A.C., McLure, R.J., Pentericci, L., 2023. A new measurement of the expansion history of the Universe at z = 1.26 with cosmic chronometers in VANDELS. Astron. Astrophys. 679, A96. https://doi.org/10.1051/0004-6361/202346992. arXiv:2305.16387.

Vagnozzi, S., Di Valentino, E., Gariazzo, S., Melchiorri, A., Mena, O., Silk, J., 2021a. The galaxy power spectrum take on spatial curvature and cosmic concordance. Phys. Dark Universe 33, 100851. https://doi.org/10.1016/j.dark.2021.100851. arXiv:2010.02230.

Vagnozzi, S., Loeb, A., Moresco, M., 2021b. Eppur è piatto? The cosmic chronometers take on spatial curvature and cosmic concordance. Astrophys. J. 908, 84. https://doi.org/10.3847/1538-4357/abd4df. arXiv:2011.11645.

van Eerten, H., 2014. Gamma-ray burst afterglow plateau break time–luminosity correlations favour thick shell models over thin shell models. Mon. Not. R. Astron. Soc. 445, 2414–2423. https://doi.org/10.1093/mnras/stu1921. arXiv:1404.0283.

Verde, L., Bernal, J.L., Heavens, A.F., Jiménez, R., 2017. The length of the low-redshift standard ruler. Mon. Not. R. Astron. Soc. 467, 731–736. https://doi.org/10.1093/mnras/stx116. arXiv:1607.05297.

Verde, L., Treu, T., Riess, A.G., 2019. Tensions between the early and the late Universe. Nat. Astron. 3, 891. https://doi.org/10.1038/s41550-019-0902-0. arXiv:1907.10625.

Verde, L., Schöneberg, N., Gil-Marín, H., 2023. A tale of many H_0. arXiv:2311.13305.

Wang, F., Dai, Z., Liang, E., 2015. Gamma-ray burst cosmology. New Astron. Rev. 67, 1–17.

Wang, F.Y., Hu, J.P., Zhang, G.Q., Dai, Z.G., 2022. Standardized long gamma-ray bursts as a cosmic distance indicator. Astrophys. J. 924, 97. https://doi.org/10.3847/1538-4357/ac3755.

Wang, Y.Y., Wang, F., 2019. Calibration of gamma-ray burst luminosity correlations using gravitational waves as standard sirens. Astrophys. J. 873, 39.

Yonetoku, D., Murakami, T., Nakamura, T., Yamazaki, R., Inoue, A.K., Ioka, K., 2004. Gamma-ray burst formation rates inferred from the spectral peak energy-peak luminosity relation. Astrophys. J. 609, 935. https://doi.org/10.1086/421285. arXiv:astro-ph/0309217.

Yu, H., Ratra, B., Wang, F.Y., 2018. Hubble parameter and baryon acoustic oscillation measurement constraints on the Hubble constant, the deviation from the spatially flat ΛCDM model, the deceleration–acceleration transition redshift, and spatial curvature. Astrophys. J. 856, 3. https://doi.org/10.3847/1538-4357/aab0a2. arXiv:1711.03437.

Zhang, B., Meszaros, P., 2001. Gamma-ray burst afterglow with continuous energy injection: signature of a highly magnetized millisecond pulsar. Astrophys. J. Lett. 552, L35–L38. https://doi.org/10.1086/320255. arXiv:astro-ph/0011133.

Zhang, C., Zhang, H., Yuan, S., Zhang, T.J., Sun, Y.C., 2014. Four new observational $H(z)$ data from luminous red galaxies in the Sloan Digital Sky Survey data release seven. Res. Astron. Astrophys. 14, 1221–1233. https://doi.org/10.1088/1674-4527/14/10/002. arXiv:1207.4541.